The Astrophysical Journal Supplement Series, 227:25 (25pp), 2016 December doi:10.3847/1538-4365/227/2/25

WEAK AND COMPACT RADIO EMISSION IN EARLY HIGH-MASS STAR-FORMING REGIONS. I. VLA OBSERVATIONS

V. Rosero[1,2], P. Hofner[1,8], M. Claussen[2], S. Kurtz[3], R. Cesaroni[4], E. D. Araya[5], C. Carrasco-González[3], L. F. Rodríguez[3], K. M. Menten[6], F. Wyrowski[6], L. Loinard[3,6], and S. P. Ellingsen[7]
[1] Physics Department, New Mexico Tech, 801 Leroy Pl., Socorro, NM 87801, USA
[2] National Radio Astronomy Observatory, 1003 Lopezville Rd., Socorro, NM 87801, USA
[3] Instituto de Radioastronomía y Astrofísica, Universidad Nacional Autónoma de México, Morelia 58090, México
[4] INAF, Osservatorio Astrofisico di Arcetri, Largo E. Fermi 5, I-50125 Firenze, Italy
[5] Physics Department, Western Illinois University, 1 University Circle, Macomb, IL 61455, USA
[6] Max-Planck-Institute für Radioastronomie, Auf dem Hügel 69, D-53121 Bonn, Germany
[7] School of Physical Sciences, University of Tasmania, Private Bag 37, Hobart, Tasmania 7001, Australia
Received 2016 April 25; revised 2016 August 30; accepted 2016 August 31; published 2016 December 9

ABSTRACT

We present a high-sensitivity radio continuum survey at 6 and 1.3 cm using the Karl G. Jansky Very Large Array toward a sample of 58 high-mass star-forming regions. Our sample was chosen from dust clumps within infrared dark clouds with and without IR sources (CMC–IRs and CMCs, respectively), and hot molecular cores (HMCs), with no previous, or relatively weak radio continuum detection at the 1 mJy level. Due to the improvement in the continuum sensitivity of the Very Large Array, this survey achieved map rms levels of ∼3–10 μJy beam^{-1} at subarcsecond angular resolution. We extracted 70 continuum sources associated with 1.2 mm dust clumps. Most sources are weak, compact, and prime candidates for high-mass protostars. Detection rates of radio sources associated with the millimeter dust clumps for CMCs, CMC–IRs, and HMCs are 6%, 53%, and 100%, respectively. This result is consistent with increasing high-mass star formation activity from CMCs to HMCs. The radio sources located within HMCs and CMC–IRs occur close to the dust clump centers, with a median offset from it of 12,000 au and 4000 au, respectively. We calculated 5–25 GHz spectral indices using power-law fits and obtained a median value of 0.5 (i.e., flux increasing with frequency), suggestive of thermal emission from ionized jets. In this paper we describe the sample, observations, and detections. The analysis and discussion will be presented in Paper II.

Key words: radio continuum: ISM – ISM: jets and outflows – stars: formation – stars: massive – techniques: interferometric

Supporting material: machine-readable tables

1. INTRODUCTION

High-mass stars ($M \gtrsim 8\,M_{\odot}$) are rare, they evolve on short timescales, and they are usually born in clusters located in highly obscured, and distant (typically >1 kpc) regions. These observational challenges have made the study of their earliest evolutionary phases difficult. The population of high-mass stars in the Galaxy has been probed by centimeter-wavelength radio continuum emission at least since the early single dish compact H II regions surveys (e.g., Mezger & Henderson 1967). Subsequent interferometric surveys (e.g., Wood & Churchwell 1989; Garay et al. 1993; Kurtz et al. 1994) discovered even more compact emission (the so-called ultracompact, or UC H II regions), or yet denser regions of ionized gas called hypercompact H II regions (HC H II, e.g., Wilson et al. 2003; Sánchez-Monge et al. 2011). All these regions detected in the past—whether compact or ultra/hypercompact—share two important characteristics. First, they are fairly bright at radio wavelengths, with centimeter flux densities ranging from a few mJy to a few Jy. Second, they arise from a relatively late stage in the star formation process when nuclear burning likely has already begun, thus producing copious amounts of UV radiation that photoionizes the gas surrounding the young star.

Subsequently, with the goal of finding candidates of earlier evolutionary phases of high-mass star formation, researchers turned to the study of dense condensations in molecular clouds. In this paper we will refer to molecular (or dust) *clumps* as structures of ∼1 pc, which are typically probed by millimeter single dish studies (e.g., Beuther et al. 2002a; Rathborne et al. 2006). In addition, we will refer to *cores* as substructures of size ∼0.1 pc that are found within clumps and are typically probed by radio/millimeter interferometers (e.g., Kurtz et al. 2000; Cesaroni et al. 2010).

Several studies of such condensations in the 1990s led to the identification of hot molecular cores (HMCs). HMCs have a large amount of hot molecular gas ($\sim 10^2\,M_{\odot}$, $T > 100$ K; see Section 2.1). HMCs are presumably heated by one or more embedded high-mass protostars, and in general have weak or previously undetectable radio continuum emission at sensitivities of tens of μJy (e.g., Goldsmith et al. 1986; Cesaroni et al. 1991, 1992; Olmi et al. 1993; Kurtz et al. 2000, p. 299; Cesaroni 2005; Cesaroni et al. 2010). They are thus thought to represent an evolutionary phase prior to UC/HC H II regions.

Candidates for an even earlier, possibly pre-stellar phase were discovered by millimeter and submillimeter continuum studies of the so-called infrared dark clouds (IRDCs). IRDCs harbor molecular structures of similar masses and densities as HMCs (see Table 1 of Rathborne et al. 2006). However, the temperatures are much lower ($T \sim$ 10–20 K; Pillai et al. 2006a; Peretto et al. 2010), which suggests an earlier evolutionary

[8] Adjunct Astronomer at the National Radio Astronomy Observatory, 1003 Lopezville Road, Socorro, NM 87801, USA.

phase than HMCs. While clearly not all IRDCs are presently forming stars, the most massive and opaque condensations within IRDCs might form OB stars (Kauffmann & Pillai 2010).

Several studies have attempted to understand the molecular condensations where high-mass stars form and attempted to establish an evolutionary sequence for them (e.g., Molinari et al. 1996, 1998, 2000, 2008). Based on recent Very Large Array NH_3 (Sánchez-Monge et al. 2013c), and ATCA H_2O maser and centimeter continuum (Sánchez-Monge et al. 2013a) observations of a large number of high-mass star-forming candidates, these authors have suggested an evolutionary sequence from quiescent starless cores, with relatively narrow NH_3 lines and low temperatures to protostellar cores that already contain IR point sources, and show larger linewidths and temperatures, as well as the presence of ionized gas. While this classification is reasonable, we still lack an evolutionary scheme for the earliest phases of high-mass star formation.

The present work is an attempt to characterize the earliest phases (prior to UC/HC H II regions) of high-mass star formation making use of the high continuum sensitivity of the Karl G. Jansky Very Large Array (VLA).[9] A number of physical processes that cause centimeter continuum emission have been suggested to be present during early high-mass star formation. Most of these relate to the disk/flow systems that are expected around high-mass protostars. For instance, Reid et al. (2007) proposed an ionized disk around the Orion I protostar, Neufeld & Hollenbach (1996) predict weak centimeter continuum emission from disk accretion shocks, and Reid et al. (1995) detected a synchrotron jet in the W3(H_2O) protostar. Most low-mass protostars show molecular flows that are driven by ionized—mostly thermal—jets (see Guzmán et al. 2010 for a summary), and since molecular outflows are also prevalent in regions where high-mass protostellar candidates are found (e.g., Shepherd & Churchwell 1996; Zhang et al. 2001; Beuther et al. 2002b), ionized jets associated with high-mass protostars are also expected. Furthermore, Gibb & Hoare (2007) interpreted weak and compact continuum sources in S106 and S140 as equatorial ionized winds from high-mass protostars, and Tanaka et al. (2016) have predicted the existence of weak outflow-confined H II regions in the earliest phases of high-mass star formation.

At the typical distances of several kiloparsecs for high-mass star-forming regions, these processes predict flux densities in the μJy range and are now accessible to observations with the upgraded VLA. We have thus carried out a high-sensitivity (rms ~3–10 μJy beam^{-1}) VLA survey to search for radio continuum emission at 6 and 1.3 cm with sub-arcsecond angular resolution toward candidates of high-mass star-forming sites at evolutionary phases earlier than UC and HC H II regions. In this paper we present our VLA radio continuum survey of 58 regions selected from the literature that had no previous, or relatively weak radio continuum detection at the 1 mJy level. Below we describe the sample and the observations, present the detections, and describe their physical properties. The analysis, interpretation, and conclusions of this survey will be presented in V. Rosero et al. (2016, in preparation; hereafter Paper II).

[9] The National Radio Astronomy Observatory is a facility of the National Science Foundation operated under cooperative agreement by Associated Universities, Inc.

2. OBSERVATIONS AND DATA REDUCTION

2.1. Sample Selection

The main goal of this survey is to study the centimeter continuum emission from high-mass protostellar candidates. To ensure an evolutionary phase of our targets earlier than UC and HC H II regions, the most important selection criterion was the non-detection, or a very low level (<1 mJy), of emission at centimeter wavelengths. In particular, most of our targets are non-detections in the CORNISH survey (Purcell et al. 2008), which has a typical image rms of 0.3 mJy beam^{-1} at 6 cm. We have further attempted to define a sample that would represent a progression in high-mass star formation, based on FIR luminosity, mid-IR emission, and the temperature of the associated molecular and dust clumps. This resulted in a total sample of 58 targets grouped into three categories: HMCs (25 sources), cold molecular clumps with mid-IR association (CMC–IRs; 15 sources), and cold molecular clumps (CMCs; 18 sources) devoid of IR associations. We note that our sample is not strictly defined in a statistical sense, as it contains a number of biases. Rather, a variety of prominent sources were included to search for radio counterparts. However, while our classification cannot be considered completely accurate, it does follow the trend of increasing star-forming activity from CMCs to HMCs. Our approximate classification scheme is similar to the one used by Sánchez-Monge et al. (2013c). Below we briefly comment on the properties of the three groups.

1. HMCs: these are high-luminosity ($>10^3\,L_\odot$) *IRAS* sources associated with dense gas, outflows, and masers, and that have dust and gas temperatures ~20 K on the 1 pc clump scale (Molinari et al. 1996; Sridharan et al. 2002). Many HMCs have recently been studied interferometrically in high-excitation molecular lines (e.g., Cesaroni et al. 2010; Hernández-Hernández et al. 2014). These studies showed that on the core scale (0.1 pc), HMCs have temperatures >100 K, masses of $\sim 10^2\,M_\odot$ and densities of $\approx 10^7$ cm^{-3}. For further information on HMC properties see Rathborne et al. (2006) and the references therein. The current interpretation is that HMCs contain highly embedded—possibly still accreting—high-mass stars, just prior to the development of an UC/HC H II region. Twenty-three HMCs in our sample were selected from Sridharan et al. (2002); one is an IRDC HMC from Rathborne et al. (2011) and G23.01-0.41 is a high-mass protostar with a rotating toroid, 4.5 μm excess emission, and rich maser activity (e.g., Araya et al. 2008; Furuya et al. 2008; Sanna et al. 2014).
2. CMC–IRs: representing an earlier evolutionary phase of high-mass star formation, they are cold ($T < 25$ K), massive ($M > 100\,M_\odot$) clumps found by *MSX* and *Spitzer* IRDC surveys. Rathborne et al. (2006) presented extensive 1.2 mm mapping, and Chambers et al. (2009) found that ≈50% of these clumps showed signs of early stellar activity as revealed by *Spitzer*. CMC–IRs are clumps associated with a 24 μm point source and in most cases are also associated with 4.5 μm excess emission, likely tracing shocked gas (Smith et al. 2006; Cyganowski et al. 2008). These clumps are expected to contain high-mass protostellar objects that are still in the process of accretion, and that have not substantially heated the molecular environment (e.g., G11.11-0.12P1, Rosero

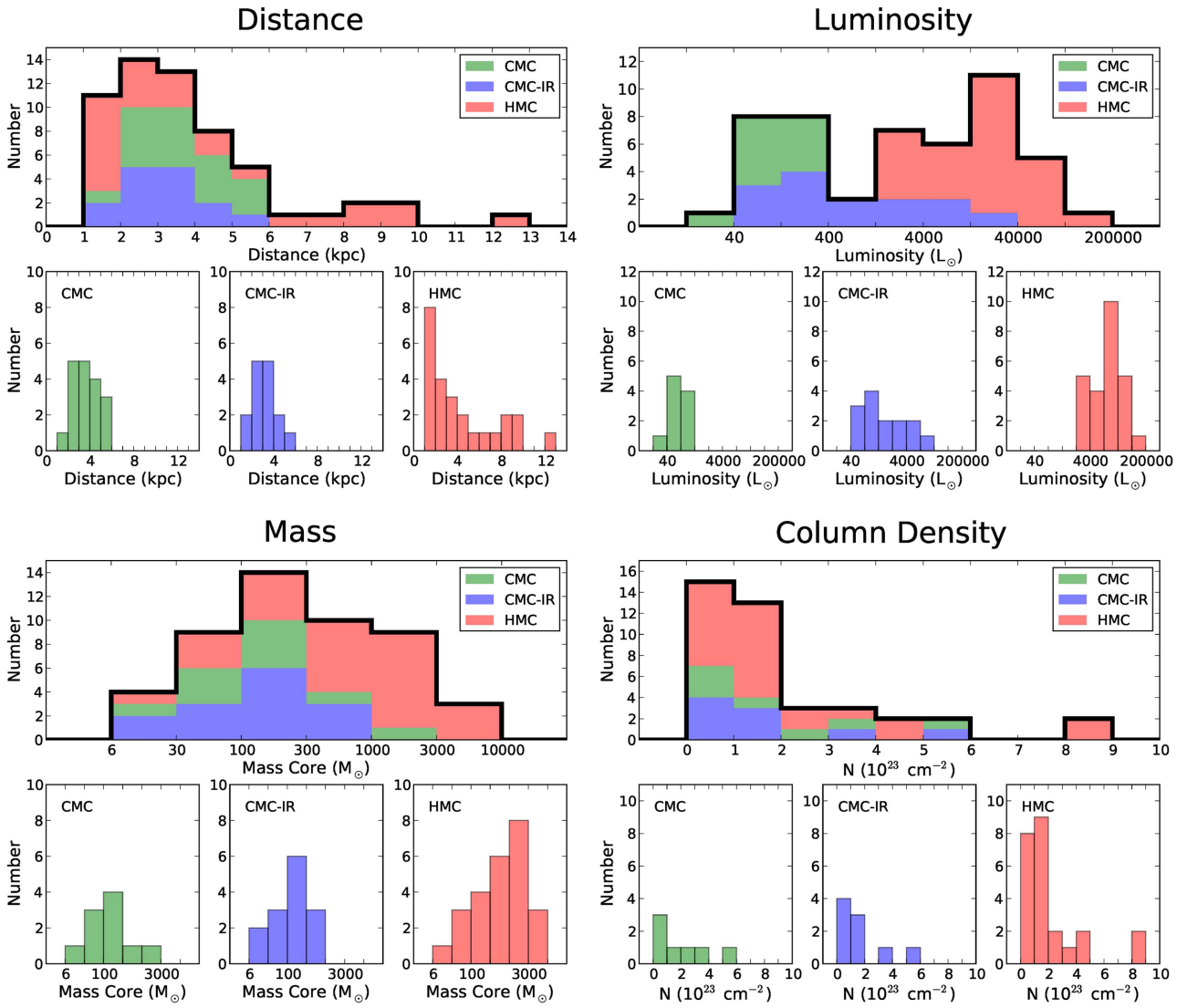

Figure 1. Distribution of kinematic distance, bolometric luminosity, mass, and column density (N) for our targets. All values were taken from the literature (see Table 1 for references). In each case the top panels correspond to the distribution of the sum of the corresponding parameter, and the bottom panels show the distribution for each type of clump independently. We use the near distance for five sources that have a kinematic distance ambiguity. Values of masses from Beuther et al. (2002a) were scaled following Beuther et al. (2005). For the total sample, nine sources do not have available values for mass and luminosity.

et al. 2014). We selected 10 CMC–IRs from Rathborne et al. (2006) and 5 additional CMC–IRs were selected from other studies (Pillai et al. 2006b; Beuther et al. 2010; Linz et al. 2010; Olmi et al. 2010).

3. CMCs: the sources from this target group were mainly selected from the original sample of Rathborne et al. (2006), the distinction being that no mid-IR source was reported by Chambers et al. (2009). The flux upper limits at 24 μm are typically <90 mJy (except for G53.11 +00.05 mm2; Rathborne et al. 2010). The absence of mid-IR sources in these massive cold clumps is consistent with a pre-stellar phase, possibly at the onset of collapse. We note that often CMCs are accompanied by CMC–IRs within the same IRDC, hence star formation is apparently occurring in their neighborhood, which could influence the (future) star formation activity within the CMCs. In total, we selected 15 CMCs from Rathborne et al. (2006) and 3 more were selected from the starless clump candidates in Vulpecula (Olmi et al. 2010).

In Figure 1 we show the distribution of kinematic distances, bolometric luminosities (estimated from *IRAS*, *Spitzer*, and *Herschel*), masses, and column densities for our sample. The data are taken from the literature; references are given in Table 1. The majority of the sources are at distances between 1 and 6 kpc, but some HMCs are as distant as ∼12 kpc (see Figure 1). The bolometric luminosity spans four orders of magnitude, with a clear separation between the low luminosity CMCs and the high-luminosity HMCs. The CMC–IRs straddle this range. The HMCs tend to be more massive, whereas the CMCs and CMC–IRs have a similar mass distribution. The range of column densities in the three types of sources is 1.8×10^{22}–8.5×10^{23} cm^{-2}. The majority of sources have sufficiently high column density to warrant high-mass star formation (Krumholz & McKee 2008; López-Sepulcre et al. 2010).

Table 1
Observed Clumps

Region	Band	R.A. (J2000)	Decl. (J2000)	ℓ (deg)	b (deg)	Beam Size ($''$ × $''$, deg)	rms (μJy beam^{-1})	Detection	Type	Distance (kpc)	L (10^3 $L_\odot$)	References
LDN1657A-3	C	07 05 00.7	−12 16 45	225.399	−2.608	0.54 × 0.28, −34.4	4.0	D	CMC–IR	1.0	…	(1)
	K					0.45 × 0.29, −4.7	12.5					
UYSO1	C	07 05 10.8	−12 18 59	225.451	−2.588	0.54 × 0.27, −35.4	4.0	D	CMC–IR	1.0	0.24	(1), (2)
	K					0.45 × 0.29, −4.4	13.0					
G11.11-0.12P1	C	18 10 28.4	−19 22 29	11.109	−0.114	0.49 × 0.27, −7.9	5.0	D	CMC–IR	3.6	1.3	(3), (4)
	K					0.67 × 0.27, −33.4	8.0					
18089-1732	C	18 11 51.3	−17 31 29	12.889	0.489	0.46 × 0.29, −19.8	6.0	D	HMC	2.34	13.5[a]	(5), (6)
	K					0.53 × 0.29, −22.4	10.0					
G15.05+00.07 mm1	C	18 17 50.4	−15 53 38	15.006	0.009	0.45 × 0.30, −19.5	6.0	ND	CMC	2.5	0.014–0.335[a,b]	(7), (8)
	K					0.47 × 0.30, −8.7	7.0					
18151-1208	C	18 17 57.1	−12 07 22	18.340	1.772	0.41 × 0.29, −18.9	6.0	D	HMC	2.8	17.4[a]	(7), (6)
	K					0.44 × 0.32, −169.2	8.0					
G15.31-00.16 mm3	C	18 18 45.3	−15 41 58	15.281	−0.092	0.43 × 0.30, −12.4	6.0	ND	CMC	3.0	…	(7)
	K					0.54 × 0.32, −31.2	8.0					
18182-1433	C	18 21 07.9	−14 31 53	16.582	−0.047	0.42 × 0.31, −9.9	6.0	D	HMC	3.58	10	(9), (10)
	K					0.60 × 0.27, −32.9	9.5					
IRDC 18223-3	C	18 25 08.5	−12 45 23	18.606	−0.075	0.43 × 0.29, −15.5	5.0	D	CMC–IR	3.7	0.6	(11)
	K					0.48 × 0.27, −22.8	9.0					
G18.82-00.28 mm3	C	18 25 52.6	−12 44 37	18.701	−0.227	0.43 × 0.29, −11.5	5.0	ND	CMC–IR	3.7	6.5[a]	(12), (8)
	K					0.44 × 0.28, −12.2	9.0					
18264-1152	C	18 29 14.3	−11 50 26	19.883	−0.534	0.41 × 0.29, −5.6	5.0	D	HMC	3.3	13	(13)
	K					0.42 × 0.29, −4.6	9.0					
G22.35+00.41 mm1	C	18 30 24.4	−09 10 34	22.377	0.447	0.48 × 0.30, +26.5	7.0	ND	CMC–IR	3.2	0.1[a]	(14), (8)
	K					0.39 × 0.26, −13.2	15.0					
G22.73+00.11 mm1	C	18 32 13.0	−09 00 50	22.727	0.126	0.39 × 0.26, −11.4	7.0	ND	CMC	4.2	0.06[a]	(14), (8)
	K					0.48 × 0.30, +27.1	12.0					
G23.60+00.00 mm6	C	18 34 18.2	−08 18 52	23.586	−0.009	0.39 × 0.26, −10.1	7.0	ND	CMC	3.7	0.003–0.125[b]	(8)
	K					0.43 × 0.30, −20.8	9.0					
G23.01-0.41	C	18 34 40.3	−09 00 38	23.009	−0.411	0.39 × 0.26, −6.9	7.0	D	HMC	4.59	181[a]	(15), (16)
	K					0.48 × 0.30, +26.5	9.0					
G24.33+00.11 mm4	C	18 35 19.4	−07 37 17	24.317	0.086	0.38 × 0.26, −3.9	7.0	ND	CMC	3.7	0.035–0.286[b]	(8)
	K					0.42 × 0.29, −19.1	9.0					
18337-0743	C	18 36 29.0	−07 40 33	24.401	−0.194	0.38 × 0.26, −2.0	7.0	D	HMC	3.8	21	(13)
	K					0.43 × 0.29, −18.5	9.0					
18345-0641	C	18 37 16.8	−06 38 32	25.410	0.105	0.38 × 0.29, −13.7	7.0	D	HMC	5.2	15	(13)
	K					0.57 × 0.29, −39.0	30.0					
G25.04-00.20 mm1	C	18 38 10.2	−07 02 44[c]	25.153	−0.276	0.38 × 0.29, −5.4	5.0	ND	CMC–IR	4.3	0.55[a]	(12), (8)
	K					0.46 × 0.29, −30.2	9.0					
G25.04-00.20 mm3	C	18 38 10.2	−07 02 44	25.153	−0.276	0.38 × 0.30, −5.4	5.0	ND	CMC	3.5	0.01–0.31[a,b]	(14), (8)
	K					0.46 × 0.29, −30.2	9.0					
G27.75+00.16 mm2	C	18 41 33.0	−04 33 44	27.746	0.114	0.38 × 0.30 , −8.9	5.0	ND	CMC	3.5	0.2[a]	(12), (8)
	K					0.41 × 0.29, −18.2	7.0					
G28.23-00.19 mm1	C	18 43 30.7	−04 13 12	28.273	−0.164	0.36 × 0.30, −1.1	5.0	ND	CMC	4.1	0.04[a]	(14), (8)
	K					0.38 × 0.30, −3.1	7.0					
G28.23-00.19 mm3	C	18 43 30.7	−04 13 12[c]	28.273	−0.164	0.36 × 0.30, −1.1	5.0	ND	CMC	5.1	0.003–0.1[a,b]	(12), (8)
	K					0.38 × 0.30, −3.1	7.0					
G28.53-00.25 mm1	C	18 44 18.0	−03 59 34	28.565	−0.235	0.36 × 0.31, −177.2	5.0	ND	CMC	4.4	0.15[a]	(14), (8)

Table 1
(Continued)

Region	Band	R.A. (J2000)	Decl. (J2000)	ℓ (deg)	b (deg)	Beam Size ($'' \times ''$, deg)	rms (μJy beam^{-1})	Detection	Type	Distance (kpc)	L (10^3 $L_\odot$)	References
	K					0.43 × 0.32, +11.2	9.0					
G28.53-00.25 mm2	C	18 44 18.0	−03 59 34[c]	28.565	−0.235	0.36 × 0.31, −177.2	5.0	ND	CMC–IR	4.4	0.36[a]	(14), (8)
	K					0.43 × 0.32, +11.2	9.0					
G28.53-00.25 mm4	C	18 44 18.0	−03 59 34[c]	28.565	−0.235	0.36 × 0.31, −177.2	5.0	ND	CMC	5.4	0.25[a]	(12), (8)
	K					0.43 × 0.32, +11.2	9.0					
G28.53-00.25 mm6	C	18 44 18.0	−03 59 34[c]	28.565	−0.235	0.36 × 0.31, −177.2	5.0	ND	CMC	5.5	0.008–0.27[a,b]	(12), (8)
	K					0.43 × 0.32, +11.2	9.0					
18437-0216	C	18 46 22.7	−02 13 24	30.377	0.111	0.38 × 0.31, +3.27	5.5	D	HMC	7.3	25	(6)
	K					0.55 × 0.29, −41.6	20.0					
18440-0148	C	18 46 36.3	−01 45 23	30.818	0.274	0.38 × 0.30, +5.7	6.0	D	HMC	8.3	23	(6), (17)
	K					0.43 × 0.28, −31.8	10.0					
G30.97-00.14 mm1	C	18 48 22.0	−01 47 42[c]	30.984	−0.135	0.35 × 0.32, −21.0	5.0	ND	CMC–IR	5.0	4.8[a]	(12), (8)
	K					0.38 × 0.28, −21.8	9.5					
G30.97-00.14 mm2	C	18 48 22.0	−01 47 42	30.984	−0.135	0.35 × 0.32, −21.0	5.0	ND	CMC	4.8	…	(8)
	K					0.38 × 0.28, −21.8	9.5					
18470-0044	C	18 49 36.7	−00 41 05	32.114	0.094	0.33 × 0.31, −7.0	7.0	D	HMC	8.2	79	(6)
	K					0.36 × 0.29, −5.5	12.0					
G34.43+00.24 mm1	C	18 53 18.0	+01 25 24	34.411	0.235	0.33 × 0.33, −22.9	6.0	D	HMC	1.56/3.7	5.7/33	(18), (19)
	K					0.38 × 0.30, −35.7	10.0					
G34.43+00.24 mm2	C	18 53 18.0	+01 25 24[c]	34.411	0.235	0.33 × 0.33, −22.9	6.0	D	CMC–IR	3.7	14	(8)
	K					0.38 × 0.30, −35.7	10.0					
18517+0437	C	18 54 13.8	+04 41 32	37.427	1.518	0.33 × 0.32, −89.1	4.5	D	HMC	1.88	7[a]	(20), (13)
	K					0.37 × 0.30, −38.1	8.5					
18521+0134	C	18 54 40.8	+01 38 02	34.756	0.024	0.34 × 0.32, +38.4	5.0	D	HMC	9.1	63	(13)
	K					0.38 × 0.30, −34.9	9.0					
G35.39-00.33 mm2	C	18 56 59.2	+02 04 53	35.417	−0.285	0.36 × 0.32, −57.0	4.0	D	CMC–IR	2.3	1.9[a]	(14), (21)
	K					0.37 × 0.29, −36.3	9.0					
G35.59-00.24 mm2	C	18 57 07.4	+02 16 14	35.601	−0.229	0.36 × 0.33, −60.2	4.0	ND	CMC–IR	2.3	0.08[a]	(14), (8)
	K					0.37 × 0.30, −34.3	10.0					
18553+0414	C	18 57 52.9	+04 18 06	37.494	0.530	0.36 × 0.33, −69.6	4.5	D	HMC	12.3	86	(13)
	K					0.41 × 0.31, −31.4	7.0					
18566+0408	C	18 59 10.0	+04 12 14	37.553	0.201	0.36 × 0.33, +86.6	4.0	D	HMC	6.7	60	(6), (22)
	K					0.40 × 0.30, −31.3	7.0					
19012+0536	C	19 03 45.1	+05 40 40	39.387	−0.140	0.32 × 0.27, −3.6	4.0	D	HMC	4.2	19	(13)
	K					0.39 × 0.29, −30.4	7.5					
G38.95-00.47 mm1	C	19 04 07.4	+05 08 48	38.957	−0.466	0.33 × 0.28, −179.0	4.0	ND	CMC	2.1	0.02[a]	(14), (8)
	K					0.40 × 0.31, −29.3	8.0					
19035+0641	C	19 06 01.1	+06 46 35	40.621	−0.136	0.32 × 0.27, −3.4	4.0	D	HMC	2.3	8.2	(13)
	K					0.39 × 0.29, −28.6	8.0					
19266+1745	C	19 28 54.0	+17 51 56	53.032	0.117	0.31 × 0.27, −4.2	6.0	D	HMC	9.5	50	(13)
	K					0.42 × 0.36, −33.2	4.0					
G53.11+00.05 mm2	C	19 29 20.2	+17 57 06	53.157	0.067	0.31 × 0.27, −3.6	6.0	D	CMC	1.9	0.36[a]	(12), (8)
	K					0.42 × 0.36, −28.4	4.0					
G53.25+00.04 mm2	C	19 29 34.5	+18 01 39[c]	53.251	0.054	0.31 × 0.27, −2.2	6.0	D	CMC–IR	2	0.046	(12), (8)
	K					0.41 × 0.31, −60.3	10.0					
G53.25+00.04 mm4	C	19 29 34.5	+18 01 39	53.251	0.054	0.31 × 0.27, −2.2	6.0	D	CMC–IR	2	0.188	(8), (12)
	K					0.41 × 0.31, −60.3	9.0					

Table 1
(Continued)

Region	Band	R.A. (J2000)	Decl. (J2000)	ℓ (deg)	b (deg)	Beam Size ($'' \times ''$, deg)	rms (μJy beam^{-1})	Detection	Type	Distance (kpc)	L (10^3 $L_\odot$)	References
19282+1814	C	19 30 28.1	+18 20 53	53.634	0.021	0.30 × 0.26, −2.8	6.0	D	HMC	1.9/8.2	3.9/79	(6)
	K					0.41 × 0.32, −62.2	9.0					
V10	C	19 41 05.0	+23 55 22	59.708	0.576	0.31 × 0.27, −5.9	6.0	ND	CMC	2.3	0.053	(23)
	K					0.35 × 0.29, +42.5	10.0					
V11	C	19 41 36.7	+23 23 30	59.306	0.208	0.31 × 0.27, −6.8	6.0	ND	CMC–IR	2.3	0.042	(23)
	K					0.35 × 0.29, +43.4	10.0					
V27	C	19 43 04.5	+23 01 20	59.152	−0.267	0.30 × 0.28, −11.6	5.0	ND	CMC	2.3	0.054	(23)
	K					0.36 × 0.31, −64.2	8.0					
19411+2306	C	19 43 18.1	+23 13 59	59.361	−0.207	0.30 × 0.27, −0.3	5.5	D	HMC	2.9/5.8	5/20	(6)
	K					0.32 × 0.30, +1.6	8.0					
V33	C	19 43 18.0	+23 26 35	59.543	−0.103	0.30 × 0.27, −0.1	5.0	ND	CMC	2.3	0.049	(23)
	K					0.36 × 0.31, −69.9	8.0					
19413+2332	C	19 43 28.9	+23 40 04	59.759	−0.027	0.31 × 0.26, −2.7	6.5	D	HMC	1.8/6.8	2/25	(6)
	K					0.32 × 0.30, −176.2	9.0					
20126+4104	C	20 14 26.0	+41 13 33	78.122	3.633	0.33 × 0.29, +65.2	6.0	D	HMC	1.64	10	(24)
	K					0.35 × 0.24, −85.1	10.0					
20216+4107	C	20 23 23.8	+41 17 40	79.127	2.278	0.33 × 0.29, +62.8	7.0	D	HMC	1.7	3.2	(6), (19)
	K					0.36 × 0.24, −84.2	10.0					
20293+3952	C	20 31 10.7	+40 03 10	78.975	0.356	0.33 × 0.29, +60.0	7.0	D	HMC	1.3/2.0	2.5/6	(6)
	K					0.37 × 0.24, −82.1	10.0					
20343+4129	C	20 36 07.1	+41 40 01	80.828	0.568	0.32 × 0.28, +54.2	7.0	D	HMC	1.4	3.2	(6)
	K					0.36 × 0.24, −83.2	10.0					

Notes. Units of right ascension are hours, minutes, and seconds, and units of declination are degrees, arcminutes, and arcseconds. The reported coordinates correspond to where the telescope was pointed. IRDCs G25.04-00.20, G28.23-00.19, G30.97-00.14, G34.43+00.24, G53.25+00.04, and G28.53-00.25 cover multiple millimeter clumps inside the primary beam FWHM at the higher frequency (25.5 GHz). D and ND stand for centimeter detection or non-detection, respectively, at the given rms level within the millimeter clump. Most of the HMCs sources are *IRAS* names. Galactic coordinates correspond to the pointing coordinates.
[a] Luminosity is corrected for the adopted distance.
[b] Lower and upper limits of luminosity from Rathborne et al. (2006).
[c] Several sources within the 25.5 GHz primary beam; same pointing center at a nearby clump.

References. (1) Forbrich et al. (2004), (2) Linz et al. (2010), (3) Pillai et al. (2006b), (4) Henning et al. (2010), (5) Xu et al. (2011), (6) Sridharan et al. (2002), (7) Sakai et al. (2012), (8) Rathborne et al. (2010), (9) Sato et al. (2014), (10) Moscadelli et al. (2013), (11) Beuther et al. (2010), (12) Sanhueza et al. (2012), (13) Lu et al. (2014), (14) Chira et al. (2013), (15) Brunthaler et al. (2009), (16) Araya et al. (2008), (17) Fazal et al. (2008), (18) Kurayama et al. (2011), (19) López-Sepulcre et al. (2011), (20) Wu et al. (2014), (21) Nguyen Luong et al. (2011), (22) Zhang et al. (2007), (23) Chapin et al. (2008), (24) Moscadelli et al. (2011).
(This table is available in machine-readable form.)

Table 2
VLA Parameters

Parameter	6 cm	1.3 cm
Center frequency (GHz)	4.9, 7.4	20.9, 25.5
Configuration	A	B
Spectral windows (per frequency)	8(×128 MHz)	8(×128 MHz)
Bandwidth (MHz)	2048	2048
Primary beam FWHM	9.′2, 6.′1	2.′2, 1.′8
Typical synthesis beam FWHM	∼0.″4 × 0.″3	∼0.″4 × 0.″3
Typical rms (μJy beam^{-1})	5	9

Note. Reported typical values of the synthesized beam and rms apply to the combined image at each band, i.e., including all data from both 1 GHz wide basebands.

2.2. VLA Observations

VLA continuum observations (project codes 10B-124 and 13B-210) at 6 and 1.3 cm were made for all sources in the sample. To achieve similar resolution and (u, v) coverage, we observed with scaled arrays, using the A configuration for 6 cm and the B configuration for 1.3 cm. A summary of the VLA observational parameters is given in Table 2. A list of phase calibrators used to make the observations at 6 and 1.3 cm is given in Table 3. 3C286 was used as a flux density calibrator for all sources except for LDN1657A-3 and UYSO1, for which 3C147 and 3C48 were used at 6 cm and 1.3 cm, respectively.

The 58 sources that we observed are summarized in Table 1. Column 1 gives the region name, and column 2 gives the band frequency, while columns 3, 4, 5, and 6 give the R.A, decl., Galactic longitude, and latitude of the pointing center. In some cases, several sources were sufficiently close to each other that they could be observed in a single pointing within the 25.5 GHz primary beam; in Table 1 this is indicated with a footnote. Columns 9, 10, 11, and 12 list whether we detected centimeter continuum sources coincident with the dust clumps mapped by Rathborne et al. (2006) and Beuther et al. (2002a)

Table 3
VLA Calibrators

Calibrator	Astrometry Precision[a]	Sources Calibrated
J1832-1035	C	18089-1732, G15.05+00.07 mm1, 18151-1208, G15.31-00.16 mm3, 18182-1433, IRDC 18223-3, G18.82-00.28 mm3, 18345-0641, 18264-1152, G25.04-00.20 mm3, G22.35+00.41 mm1, G22.73+00.11 mm1, G23.60+00.00 mm6, G23.01-0.41, G24.33+00.11 mm4, 18337-0743
J1851+0035	C	G27.75+00.16 mm2, G28.23-00.19 mm1, G28.53-00.25 mm1, 18437-0216, 18440-0148, G30.97-00.14 mm2, 18470-0044, G34.43+00.24 mm1, 18517+0437, 18521+0134, G35.39-00.33 mm2, G35.59-00.24 mm2, 18553+0414, 18566+0408, 19012+0536, G38.95-00.47 mm1, 19035+0641
J2007+4029	B	20126+4104, 20216+4107, 20293+3952, 20343+4129
J2015+3710[b]	C	20126+4104, 20216+4107, 20293+3952, 20343+4129
J1925+2106	A	19266+1745, G53.11+00.05 mm2, G53.25+00.04 mm4, 19282+1814, V10, V11, V27, 19411+2306, V33, 19413+2332
J0650-1637	A	LDN1657A-3, UYSO1
J0730-1141[b]	A	LDN1657A-3, UYSO1
J1820-2528	A	G11.11-0.12P1

Note. The phase calibrators listed were used for observations at the 6 and 1.3 cm bands, unless otherwise indicated. 3C 286 was used as a flux calibrator for all sources, except for LDN1657A-3 and UYSO1, for which 3C 147 and 3C 48 were used at 6 cm and 1.3 cm, respectively.
[a] Astrometry precision A, B, and C correspond to positional accuracies of <2 mas, 2–10 mas, and 0.01–0.15 arcsecs, respectively.
[b] Calibrator at 1.3 cm band.

Table 4
Continuum Parameters

Region	Radio Source	ν_c (GHz)	R.A. (J2000)	Decl. (J2000)	S_ν (μJy)	I_ν (μJy beam^{-1})	Morphology	mm assoc	Spectral Index
LDN1657A-3	A	4.9	07 05 00.65	−12 16 44.9	530	528	C	y[a]	−1.2(0.1)
	…	7.4	07 05 00.65	−12 16 44.9	758	732	…	…	…
	…	20.9	07 05 00.65	−12 16 45.1	103	88	…	…	…
	…	25.5	07 05 00.65	−12 16 44.9	95	90	…	…	…
	G225.394+2.597	4.9	07 05 02.53	−12 16 11.5	315	302	C	n[a]	−0.4(0.1)
	…	7.4	07 05 02.53	−12 16 11.5	172	172	…	…	…
	…	20.9	07 05 02.53	−12 16 11.5	146	146	…	…	…
	…	25.5	07 05 02.53	−12 16 11.4	137	132	…	…	…

Notes. In the morphology column C stands for compact and R stands for resolved. The uncertainty of the spectral index is 1σ statistical error from the fit. Several sources in our survey are very weak; the occasional presence of image artifacts (e.g., the emission lying in a negative bowl) inhibited in some cases an accurate measurement of the flux density S_ν. In these cases the spectral index was determined using the peak intensity I_ν instead of the total flux density.
[a] 1.2 mm continuum data is not available for this source. The association was based on a typical size for each type of clump.
[b] Non-detection. The upper limit is the 3σ value in the map.
[c] Components have a bridge-blending emission.
[d] A map at this frequency is not available.
[e] Contains embedded component B.

(This table is available in its entirety in machine-readable form.)

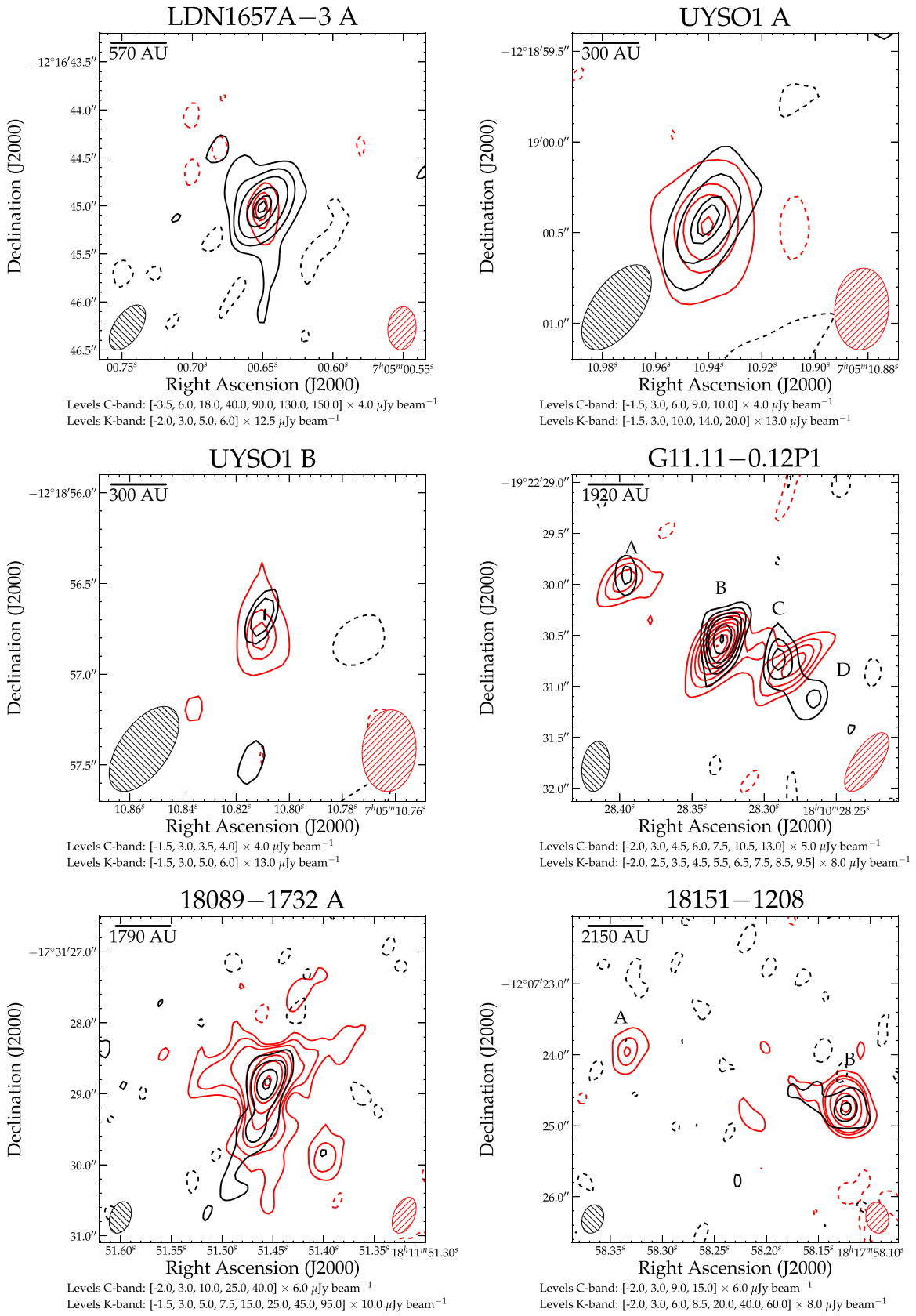

Figure 2. VLA contour plots of the 6 (black) and 1.3 (red) cm combined maps toward all sources associated with millimeter dust clumps. The synthesized beams are shown in the lower left and right corners for 6 and 1.3 cm, respectively. A scale bar in units of au is shown in the upper left. We are using the near distance for sources with distance ambiguity. There is not an available map at 1.3 cm for 19282+1814 A.

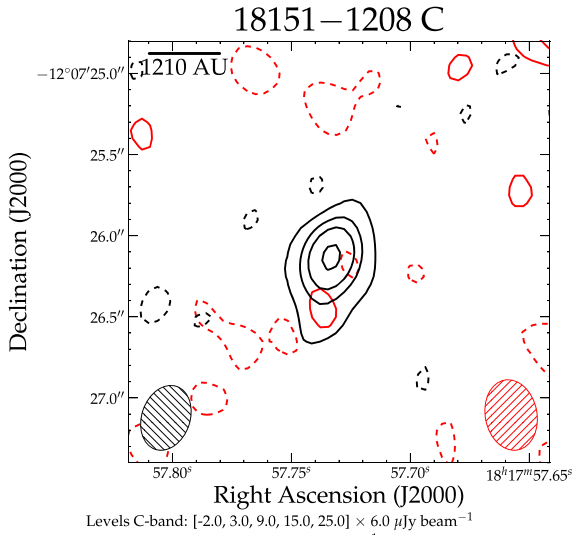

Levels C-band: [-2.0, 3.0, 9.0, 15.0, 25.0] × 6.0 μJy beam^{-1}
Levels K-band: [-1.0, 2.0] × 8.0 μJy beam^{-1}

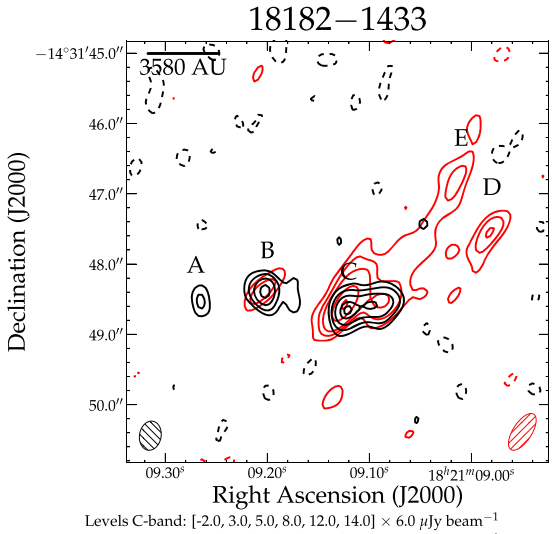

Levels C-band: [-2.0, 3.0, 5.0, 8.0, 12.0, 14.0] × 6.0 μJy beam^{-1}
Levels K-band: [-2.0, 3.0, 5.0, 8.0, 20.0, 33.0] × 9.5 μJy beam^{-1}

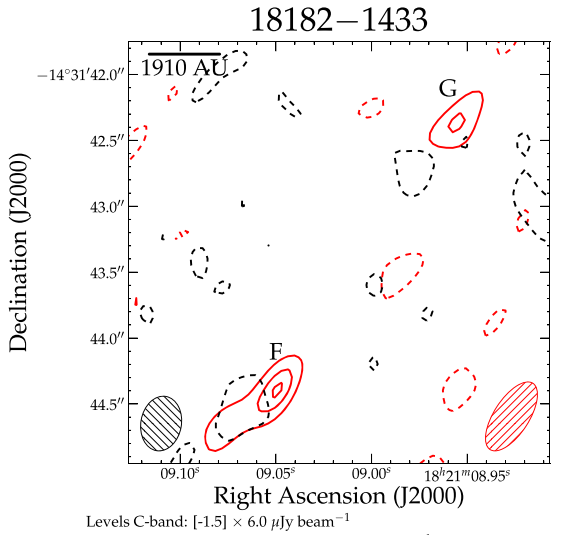

Levels C-band: [-1.5] × 6.0 μJy beam^{-1}
Levels K-band: [-1.8, 3.0, 5.0, 6.3] × 9.5 μJy beam^{-1}

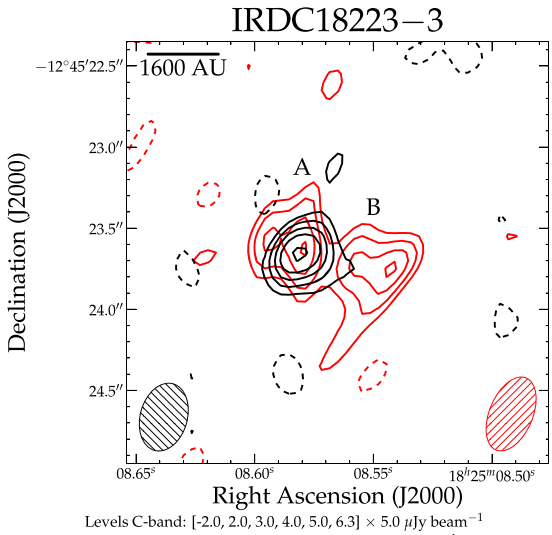

Levels C-band: [-2.0, 2.0, 3.0, 4.0, 5.0, 6.3] × 5.0 μJy beam^{-1}
Levels K-band: [-2.0, 2.0, 2.5, 3.0, 3.4] × 9.0 μJy beam^{-1}

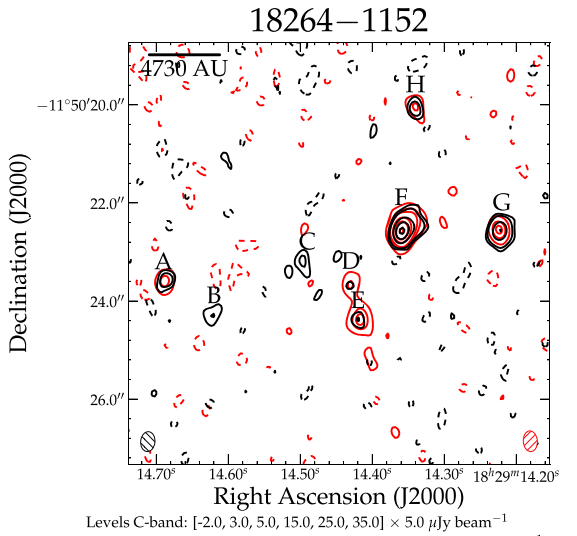

Levels C-band: [-2.0, 3.0, 5.0, 15.0, 25.0, 35.0] × 5.0 μJy beam^{-1}
Levels K-band: [-2.0, 3.0, 7.0, 10.0, 20.0, 30.0, 45.0] × 9.0 μJy beam^{-1}

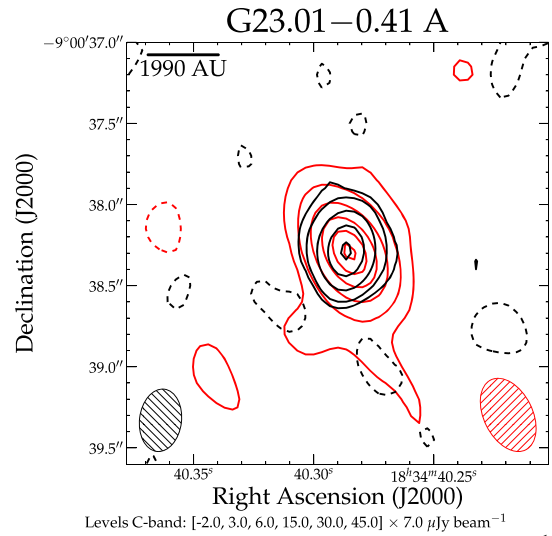

Levels C-band: [-2.0, 3.0, 6.0, 15.0, 30.0, 45.0] × 7.0 μJy beam^{-1}
Levels K-band: [-1.5, 3.0, 10.0, 25.0, 45.0, 65.0, 80.0] × 9.0 μJy beam^{-1}

Figure 2 (Continued)

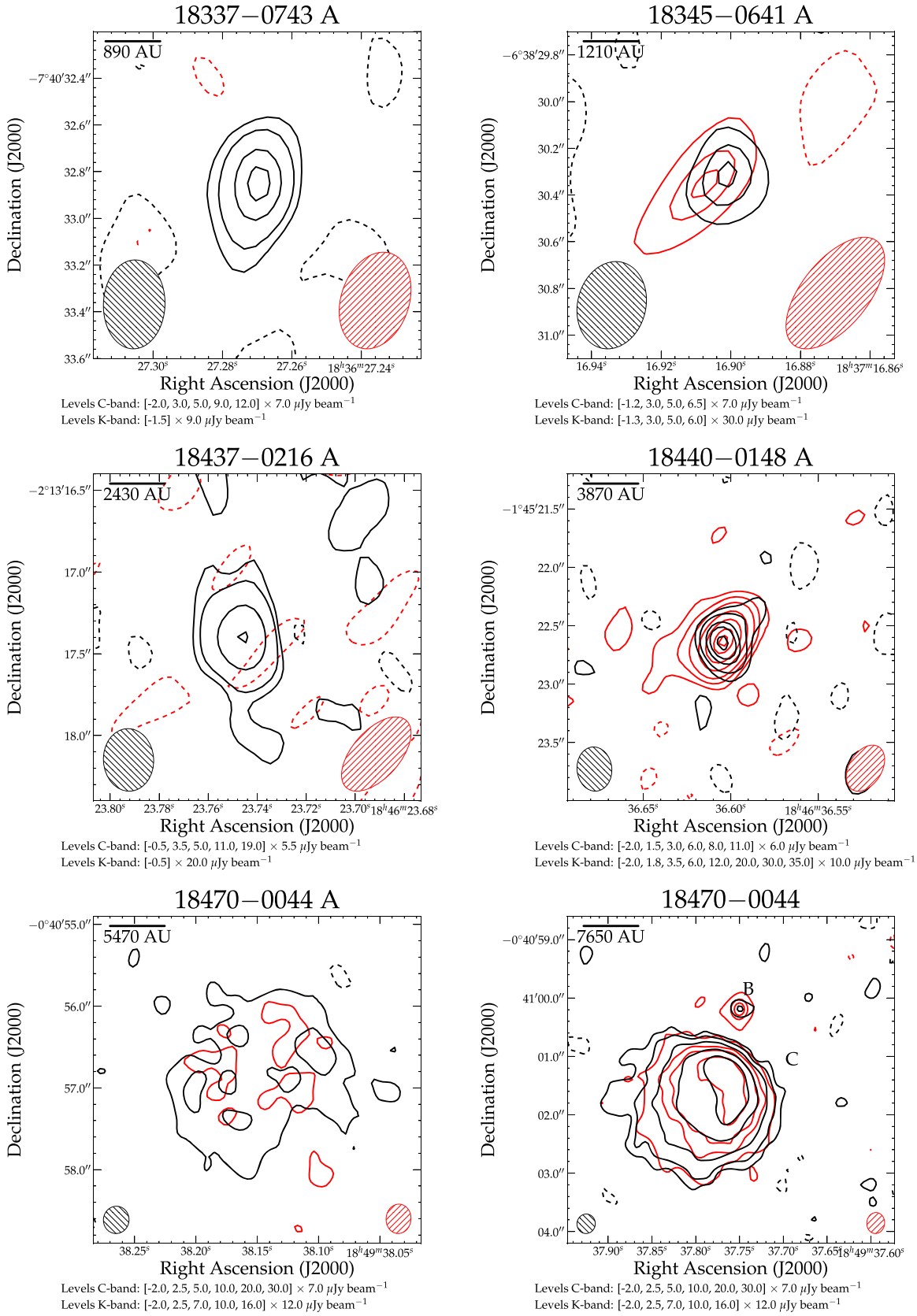

Figure 2 (Continued)

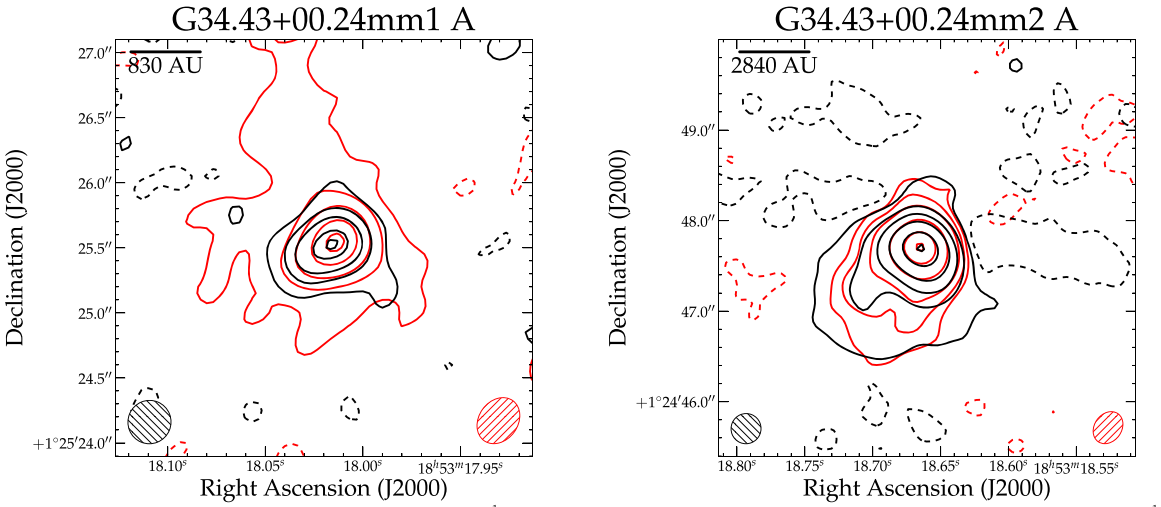

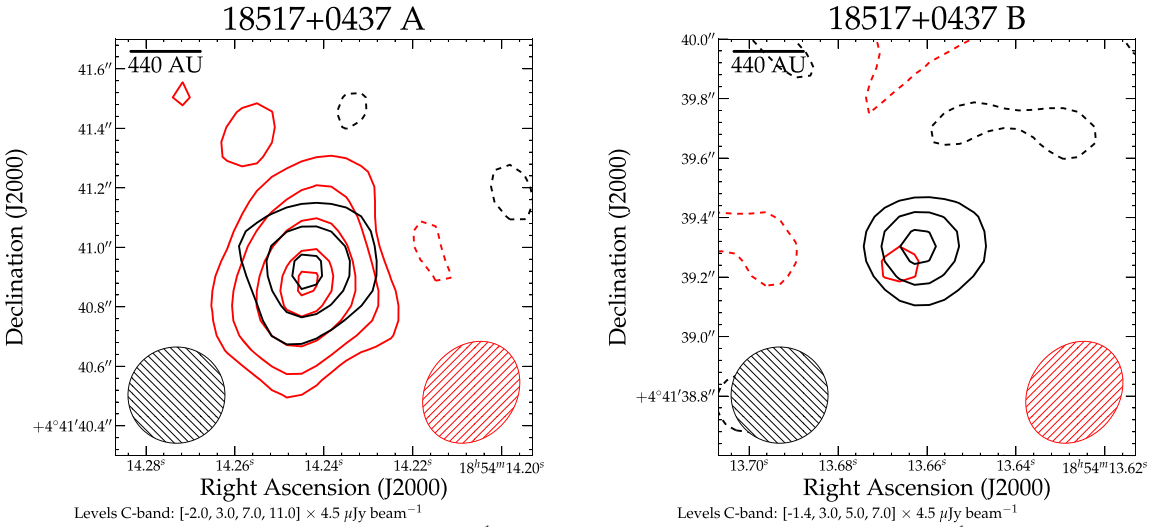

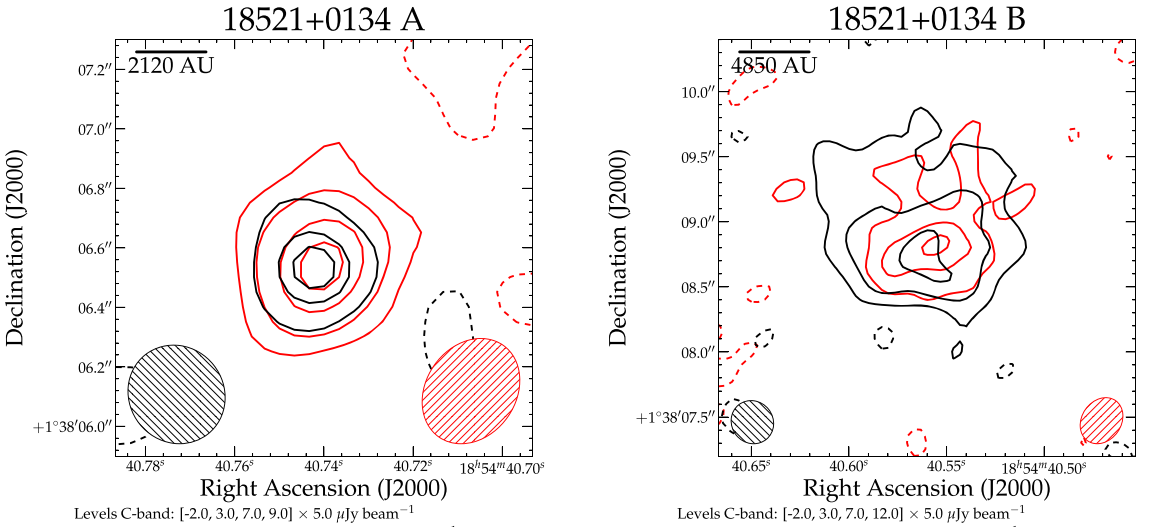

Figure 2 (Continued)

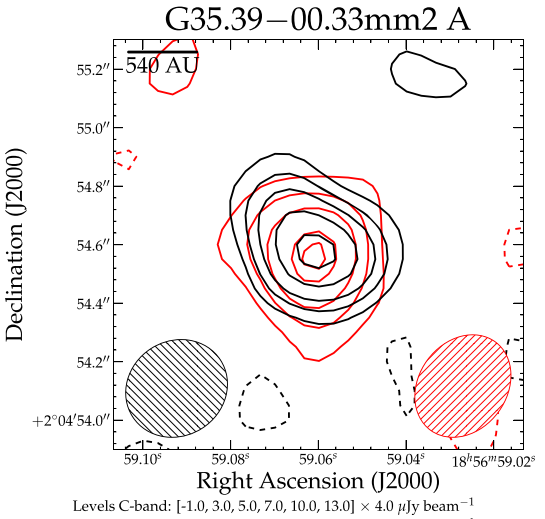

Levels C-band: [-1.0, 3.0, 5.0, 7.0, 10.0, 13.0] × 4.0 μJy beam^{-1}
Levels K-band: [-1.0, 3.0, 5.0, 7.0, 10.0, 11.0] × 9.0 μJy beam^{-1}

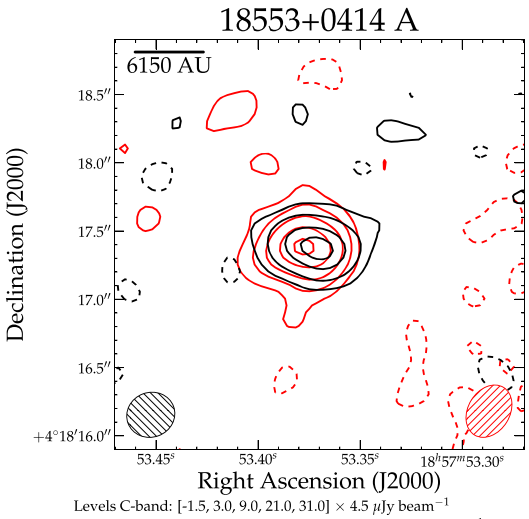

Levels C-band: [-1.5, 3.0, 9.0, 21.0, 31.0] × 4.5 μJy beam^{-1}
Levels K-band: [-1.5, 3.0, 7.0, 13.0, 21.0, 28.0] × 7.0 μJy beam^{-1}

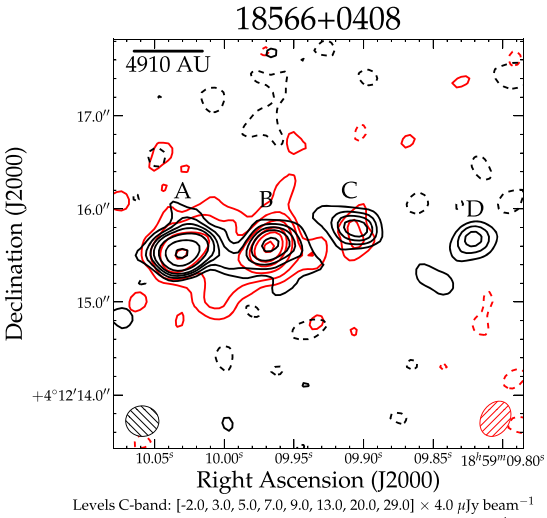

Levels C-band: [-2.0, 3.0, 5.0, 7.0, 9.0, 13.0, 20.0, 29.0] × 4.0 μJy beam^{-1}
Levels K-band: [-2.0, 3.0, 5.0, 9.0, 15.0, 20.0, 29.0] × 7.0 μJy beam^{-1}

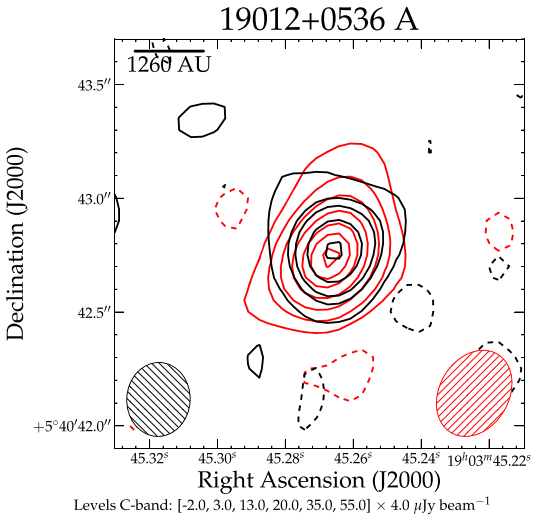

Levels C-band: [-2.0, 3.0, 13.0, 20.0, 35.0, 55.0] × 4.0 μJy beam^{-1}
Levels K-band: [-2.0, 9.0, 20.0, 35.0, 55.0, 75.0, 90.0, 105.0] × 7.5 μJy beam^{-1}

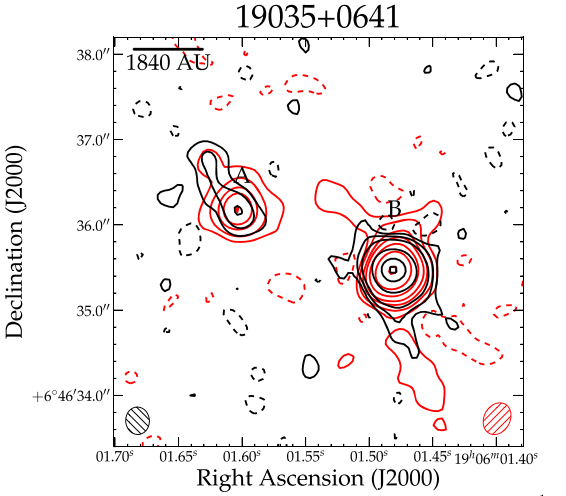

Levels C-band: [-2.5, 3.0, 10.0, 25.0, 120.0, 280.0, 380.0] × 4.0 μJy beam^{-1}
Levels K-band: [-2.0, 5.0, 10.0, 20.0, 30.0, 50.0, 90.0, 170.0] × 8.0 μJy beam^{-1}

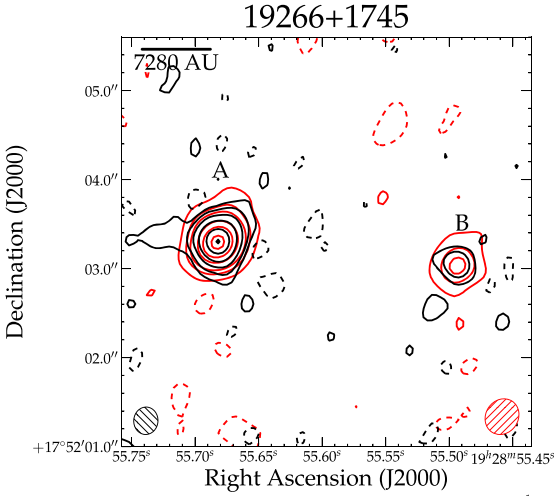

Levels C-band: [-2.5, 3.0, 8.0, 20.0, 40.0, 80.0, 118.0] × 6.0 μJy beam^{-1}
Levels K-band: [-2.0, 3.0, 10.0, 17.0, 35.0, 50.0, 70.0] × 4.0 μJy beam^{-1}

Figure 2 (Continued)

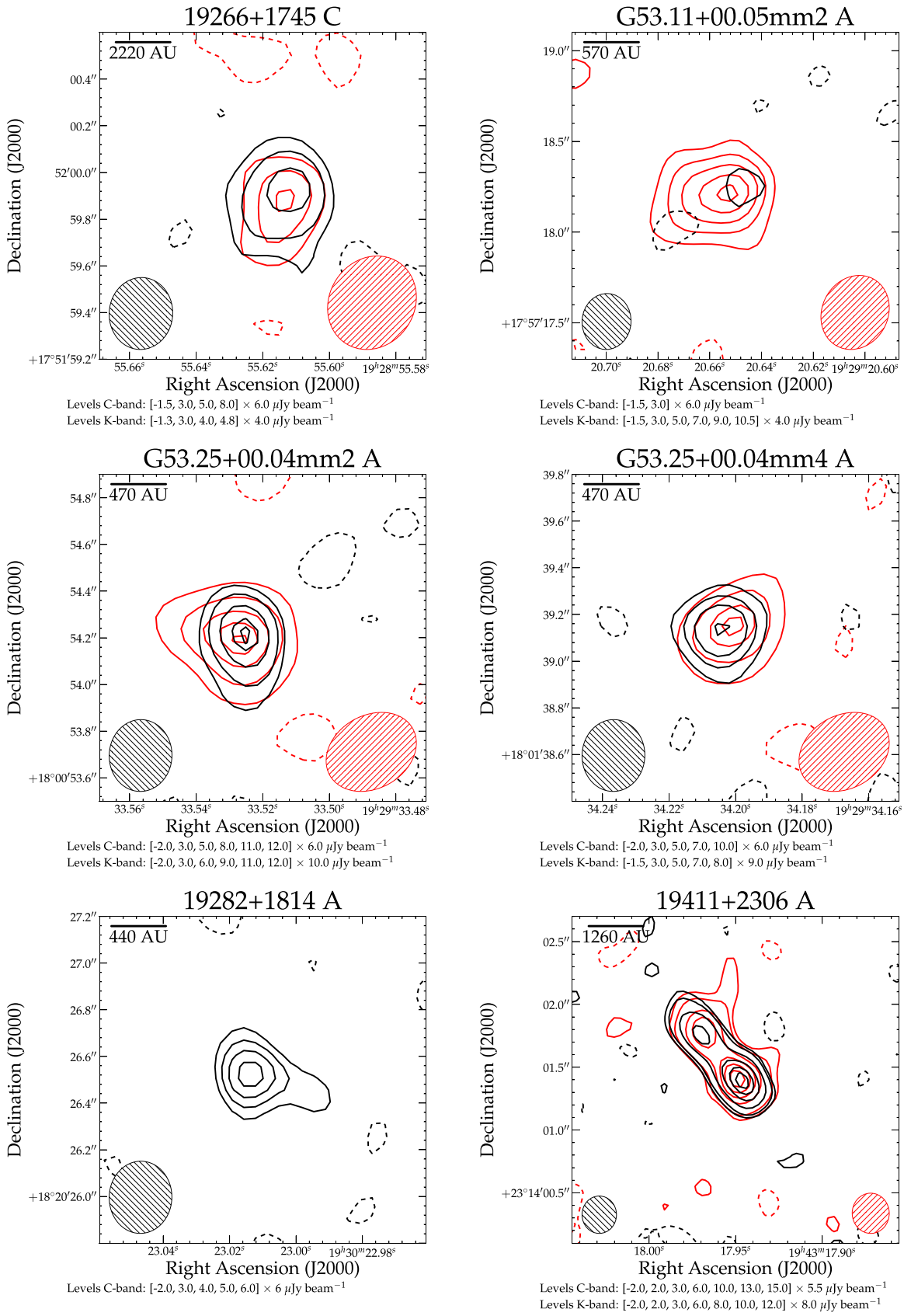

Figure 2 (Continued)

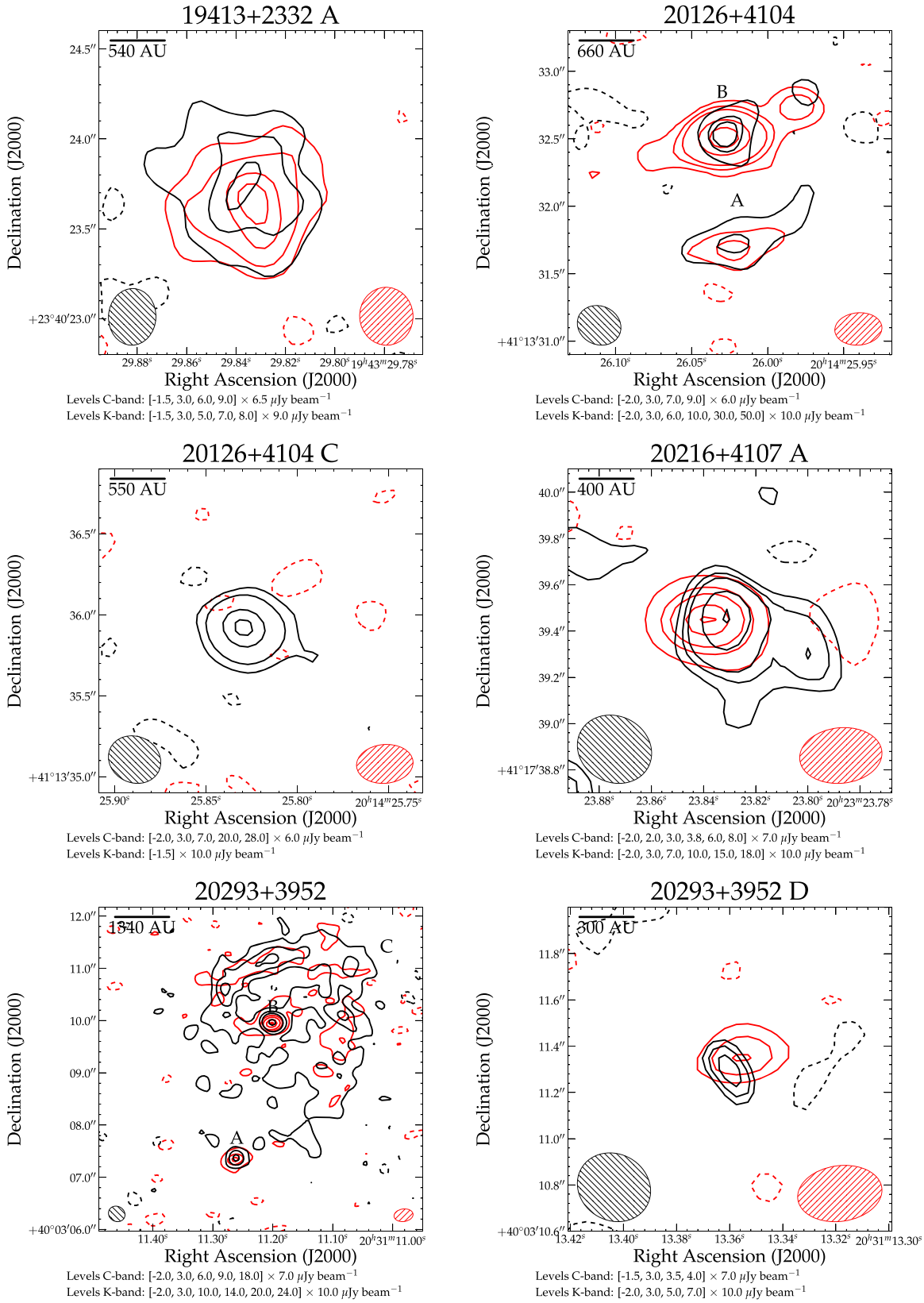

Figure 2 (Continued)

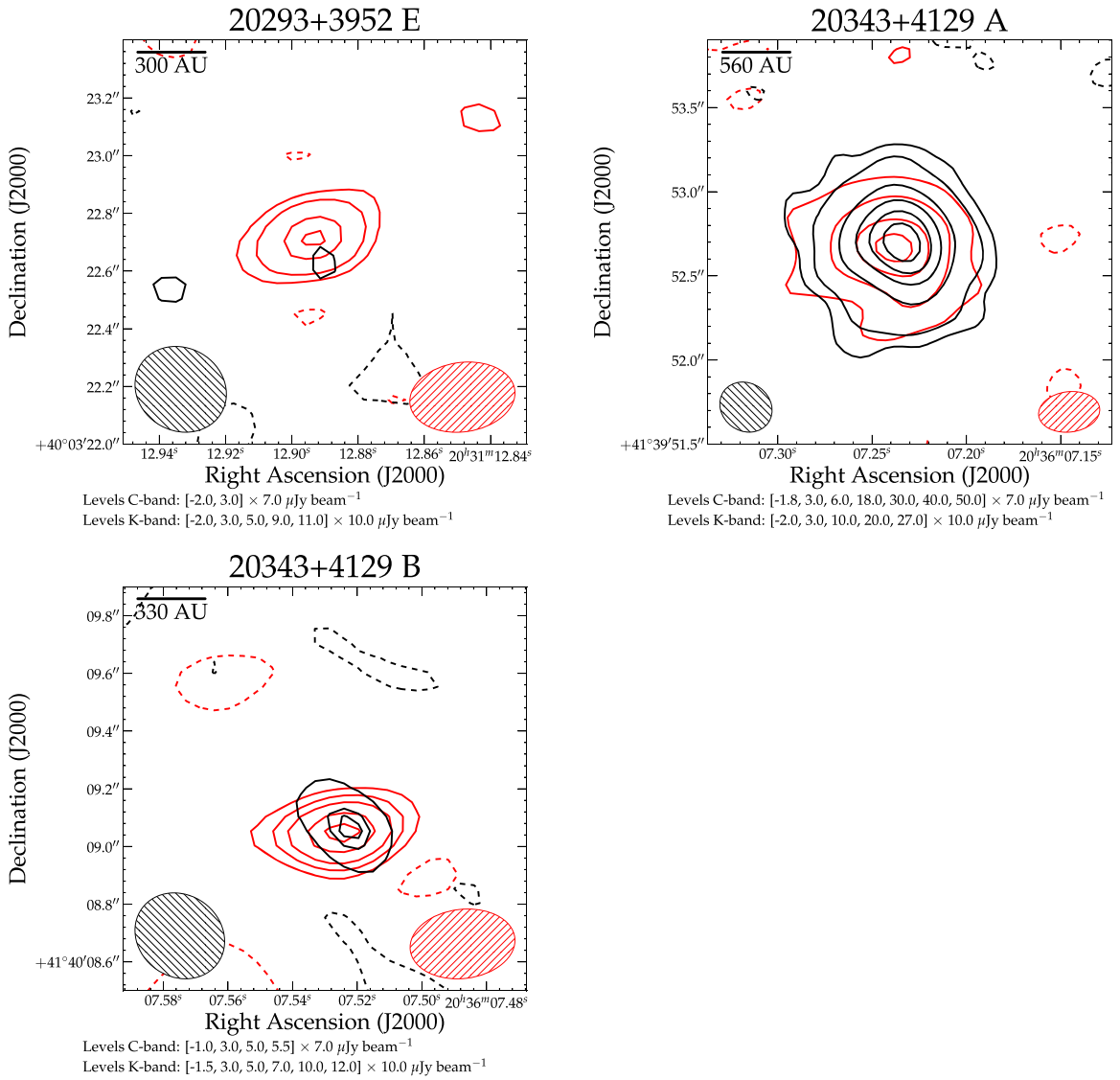

Figure 2 (Continued)

(see Section 3.1), the core/clump type, distance to the region and bolometric luminosity, respectively. Column 13 gives references for the distance and luminosity of each region.

2.2.1. 6 cm Observations

The 6 cm observations were made in the A configuration between 2011 June and August, providing a typical angular resolution of about 0.″4. Two 1 GHz wide basebands (8 bit samplers) were employed, centered at 4.9 and 7.4 GHz. Each baseband was divided into 8 spectral windows (SPWs), each with a bandwidth of 128 MHz. Therefore, the data were recorded in 16 unique SPWs, each comprised of 64 2 MHz wide channels, resulting in a total bandwidth of 2048 MHz. The SPWs were configured to avoid the strong methanol maser emission at 6.7 GHz. The observations were taken in scheduling blocks of about four regions per block, performing alternating observations on a target source for 720 s and a phase calibrator for 90 s. The typical total on-source time was ~40 minutes.

The data were processed using NRAO's Common Astronomy Software Applications (CASA)[10] package. Eight channels at the edges of each baseband were flagged due to substantial band roll-off (and therefore loss of sensitivity). In addition, we inspected the data for radio frequency interference (RFI) or other problems, performing "flagging" when needed. The flux density scale was set via standard NRAO models for the flux calibrators and using the Perley–Butler (2010) flux scale. We used the `gencal` task to check for antenna position corrections and also to apply a gain curve and antenna efficiency factors. Delay and bandpass solutions were formed based on observations of the flux density calibrator. These solutions were applied when solving for the final amplitude and phase calibration using the task `gaincal` over the full bandwidth. We measured the flux density of the phase calibrators using the task `fluxscale`. The amplitude, phase, delay, and bandpass solutions were applied to the target sources using the task `applycal`. The images were made using the `clean` task and

[10] http://casa.nrao.edu

Table 5
Summary of Detections

	CMC	CMC–IR	HMC
Number of observed regions	18	15	25
Number of regions with radio detections[a]	8	9	25
Number of regions with radio detections within the millimeter clump[b]	1	8	25
Number of radio sources detected at both 1.3 and 6 cm	2(0)	11(10)	54(40)[c]
Number of radio sources only detected at 1.3 cm	7(1)	2(2)	9(6)[c]
Number of radio sources only detected at 6 cm	7(0)	7(1)	33(10)[c]

Notes. Values in parentheses correspond to the number of sources that are within the millimeter clump; there are 70 sources in total.
[a] Any detection within the 25.5 GHz primary beam (1.′8).
[b] Only detections located within the FWHM size of the millimeter clump.
[c] Numbers do not include radio sources found in 19282+1814.

Briggs ROBUST = 0.5 weighting. Because most of the detections have low S/N (<20), no self-calibration was attempted.

As a consistency check, and to ensure the absence of line contamination or RFI, we imaged and inspected each SPW separately. Moreover, each 1 GHz baseband was imaged separately to provide a better estimate of spectral index. Finally, a combined image was made, including the data from both basebands. All maps were primary-beam-corrected. The synthesized beam size and position angle (PA) and rms noise of the combined image for each region are shown in columns 7 and 8 of Table 1.

2.2.2. 1.3 cm Observations

The 1.3 cm observations were made in the B configuration, acquiring the first half of the data between 2010 November and 2011 May, and the second half between 2013 November and 2014 January. The correlator setup was the same as that used at 6 cm, with the two basebands centered at 21 and 25.5 GHz. The observations were mostly taken in scheduling blocks of two regions each, performing alternating observations on a target source for 240 s and a phase calibrator for 60 s. The typical total on-source time was ∼40 minutes. Pointing corrections using the referenced pointing procedure were obtained every hour and were applied during the observations.

The data reduction was done in the same fashion as that for the 6 cm observations. In addition, we corrected for atmospheric opacity using the weather station information from the plotWeather task. The images were made using the clean task using natural weighting to provide the best sensitivity in the maps. As done at 6 cm, we imaged each baseband individually (for spectral index) and together (for morphology and improved S/N). All maps were primary-beam-corrected. The synthesized beam size and PA and rms noise of the combined image for each region are shown in columns 7 and 8 of Table 1.

3. RESULTS

Radio sources were identified in each of the baseband-combined images described in Section 2. The criterion adopted for defining a radio detection is that the peak intensity I_ν is $\geqslant$5 times the image rms (σ) in either the *C*- or *K*-band. Subsequently, in each 1 GHz wide band we determined the peak position, flux density S_ν, and peak brightness I_ν by enclosing each radio source in a box using the task viewer of CASA. Table 4 reports the parameters for all detected radio sources within the 1.′8 FWHM primary beam at 25.5 GHz. This table, for each observed region, lists each detected radio source, its frequency, peak position, flux density, peak intensity, morphology, millimeter clump association, and spectral index (see below). We describe the morphology either as compact (C) if the detection is apparently unresolved or shows no structure on the scale of a few synthesized beams, or resolved (R) if the detection is more extended. Several sources in our survey are very weak; the occasional presence of image artifacts (e.g., the emission lying in a negative bowl) inhibited in some cases an accurate measurement of the flux density S_ν. In these cases we only report the peak intensity I_ν (see Section 3.2). Several sources were only detected in one of the baseband-combined maps; in this case we report a 3σ limit value for the peak intensity in each 1 GHz baseband.

Since the goal of this survey was to detect radio emission from high-mass protostars we restrict the discussion to the radio sources that are associated with the dust clumps mapped by Rathborne et al. (2006) and Beuther et al. (2002a; see below). In Table 1 column 9 we indicate whether there are radio sources coincident with these millimeter clumps. To distinguish these sources further, in Table 4 for each region we label radio detections that are located within the millimeter clump with capital letters, i.e., "A," "B," "C," etc., from east to west. Sources that are within the 25.5 GHz FWHM primary beam but outside of the millimeter clump are labeled by their

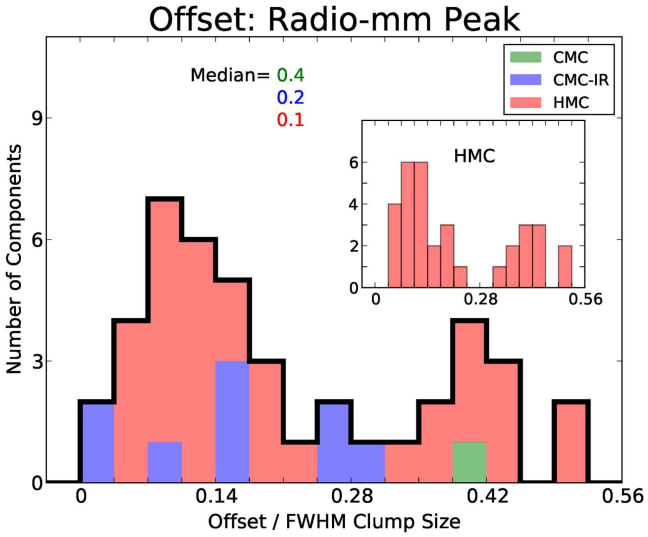

Figure 3. Position offsets between radio sources and the 1.2 mm peaks divided by the FWHM size of each clump. The inset shows the distribution only for the HMC detections. If no 1.2 mm data were available, we used the median FWHM size for the specific type of clump. The median FWHM sizes for each type of clump in this sample are 31″, 25″, and 18″ for CMCs, CMC–IRs, and HMCs, respectively. The average centimeter positional accuracy is better than 0.1″, and the typical positional accuracy for the 1.2 mm data is a few arcseconds. Clumps with multiple components (within a radius of 3″) have been treated as a single radio source in this histogram. Using a Kolmogorov–Smirnov test to analyze the spatial offset distribution of the HMCs and CMC–IRs, we estimated a *p*-value = 0.34. Thus, there is no strong evidence that these two distributions are different.

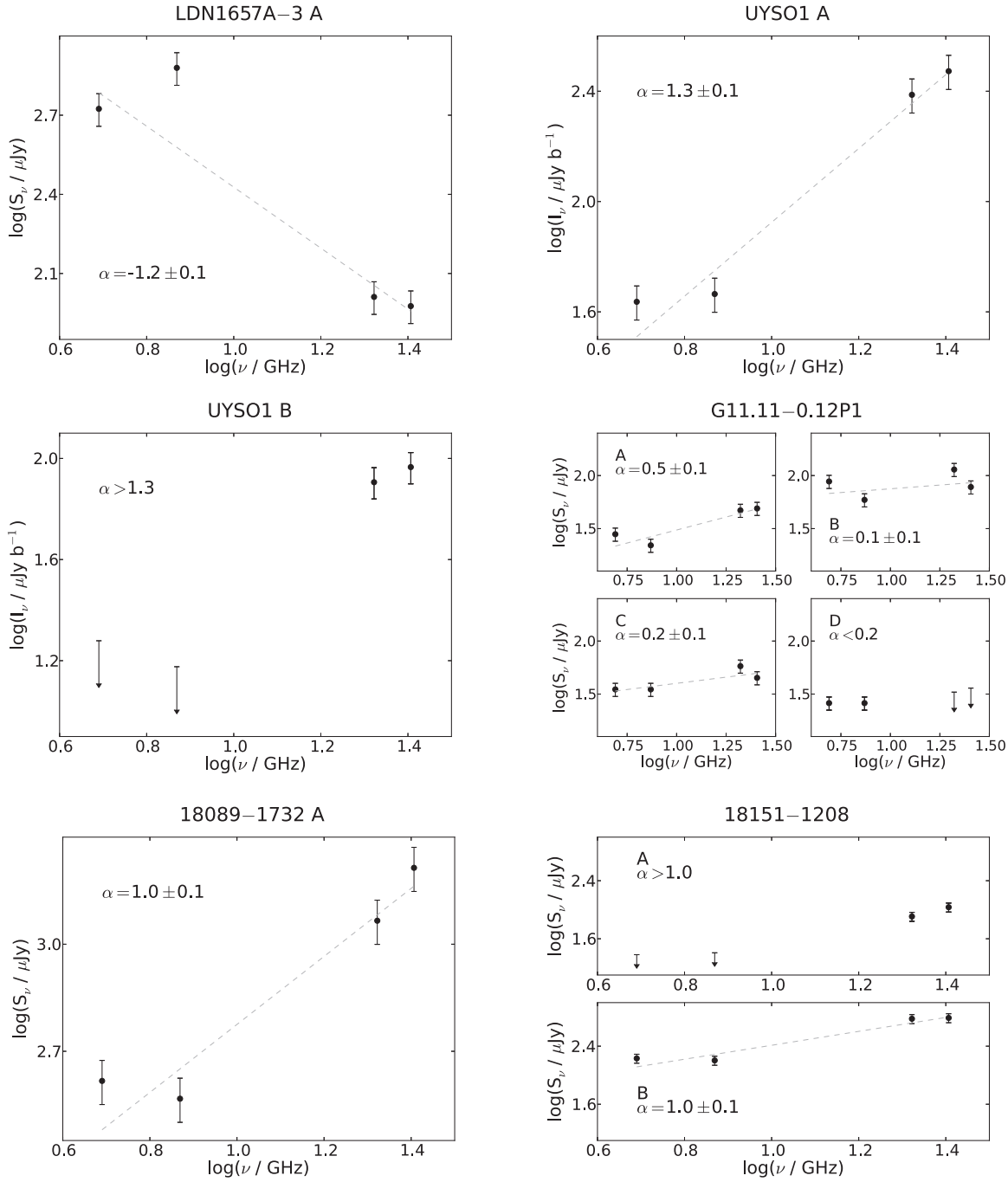

Figure 4. Flux density as a function of frequency for each detected component. Error bars are an assumed uncertainty of 10% from the flux densities added in quadrature with an assumed 10% error in calibration. The dashed lines are the best fit to the data from a power law of the form $S_\nu \propto \nu^\alpha$.

Galactic coordinates. Contour images for all radio sources associated with millimeter clumps are shown in Figure 2.

At the very low rms values of this survey many radio sources were detected; this is particularly the case in the 6 cm maps, due to their large primary beam (9.′2 at 4.9 GHz). Hence it is necessary to consider background contamination by extragalactic radio sources. At 6 cm, above a 5σ flux density of 25 μJy, we expect 0.52 extragalactic radio sources per arcmin^{-2} (Fomalont et al. 1991). Indeed, several of these radio sources, mainly outside of the primary beam, show double lobed morphologies that are typical of radio galaxies. At the typical dust clump size of ∼30″, we thus expect to detect about 0.13 sources on average in the 6 cm maps. Since we observed a total of 58 clumps, we expect to have about eight extragalactic sources in the entire sample.

To quantify this number for the 1.3 cm bands, we use the 2 cm source counts model from de Zotti et al. (2005) scaled to the 10C survey source counts by AMI Consortium et al. (2011). The average rms noise from our data at 1.3 cm is ∼9 μJy beam^{-1} and from this model we predict that we should see 0.12 sources arcmin^{-2}, or ∼0.4 radio sources within the 1.′8 FWHM primary beam of the 25.5 GHz maps above a 5σ flux density of 45 μJy. Therefore, within the millimeter clump regions at an average size of ∼30″ the likelihood of detecting

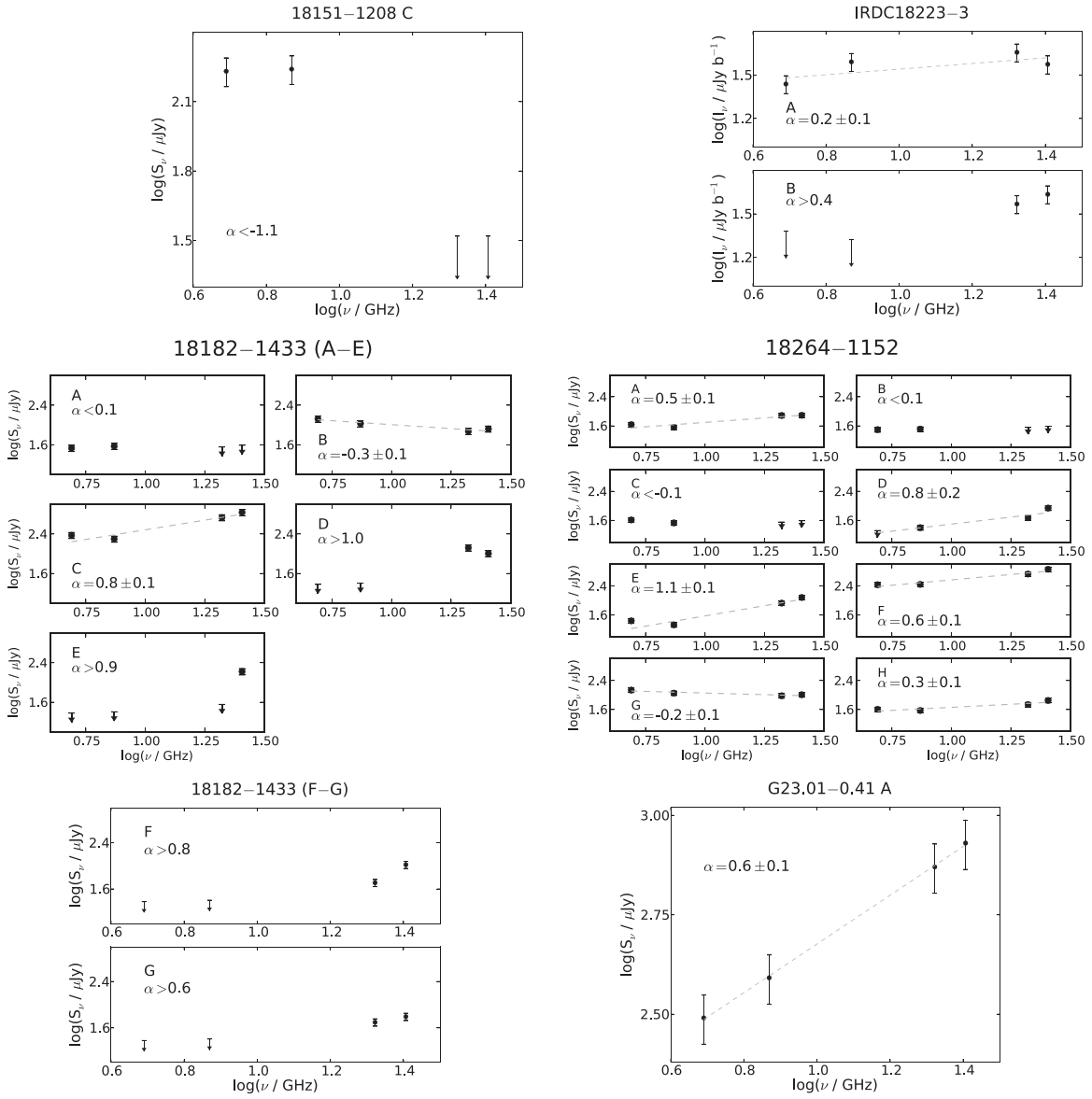

Figure 4 (Continued)

extragalactic sources is low (∼0.03 radio sources per clump) at 1.3 cm. Since we observed a total of 58 clumps, we expect to have about 2 extragalactic sources in the entire sample.

Of the 58 dust clumps we observed, we did not detect radio sources toward 24 of them. For the remaining 34 dust clumps, we report a total of 70 radio sources associated with the dust clumps (see Section 3.1), often finding 2 or more sources within a single clump (see Section 3.3). We also report a total of 62 sources[11] that are outside the radius of the millimeter clump but within the 25.5 GHz primary beam. The detection statistics for the sample are summarized in Table 5.

3.1. Association with Millimeter Clumps

Among the detections we have sources associated with dense gas traced by dust millimeter emission, and that are therefore likely part of the star-forming region. The 1.2 mm clump data were taken from Rathborne et al. (2006) and Beuther et al. (2002a) for the IRDC clumps and HMCs, respectively, except for some individual sources. We classified a radio source as associated with the 1.2 mm clumps if it was located within the FWHM of the dust emission. Toward the dust millimeter clumps we detected radio continuum emission in 1/18 (6%) of CMCs, 8/15 (53%) of CMC–IR, and 25/25 (100%) of HMCs, with a total of 70 detections. This detection statistics follows the expected trend of increasing star formation activity from CMCs to HMCs, i.e., in more evolved regions the probability of detecting weak and compact radio sources is higher than in less evolved regions.

Our data, in conjunction with the 1.2 mm maps, allow us to check where star formation occurs within the clumps. Figure 3 shows the distribution of position offsets between radio sources and the peak of the 1.2 mm emission. The FWHM median angular sizes for each type of clump in this sample are 31″, 25″, and 18″ for CMCs, CMC–IRs and HMCs, respectively. When

[11] Due to a large offset of the dust clump from the pointing center, the 19282 + 1814 region has been excluded from the statistics. However, we include contour maps at 6 cm and report the radio sources detected in Table 4.

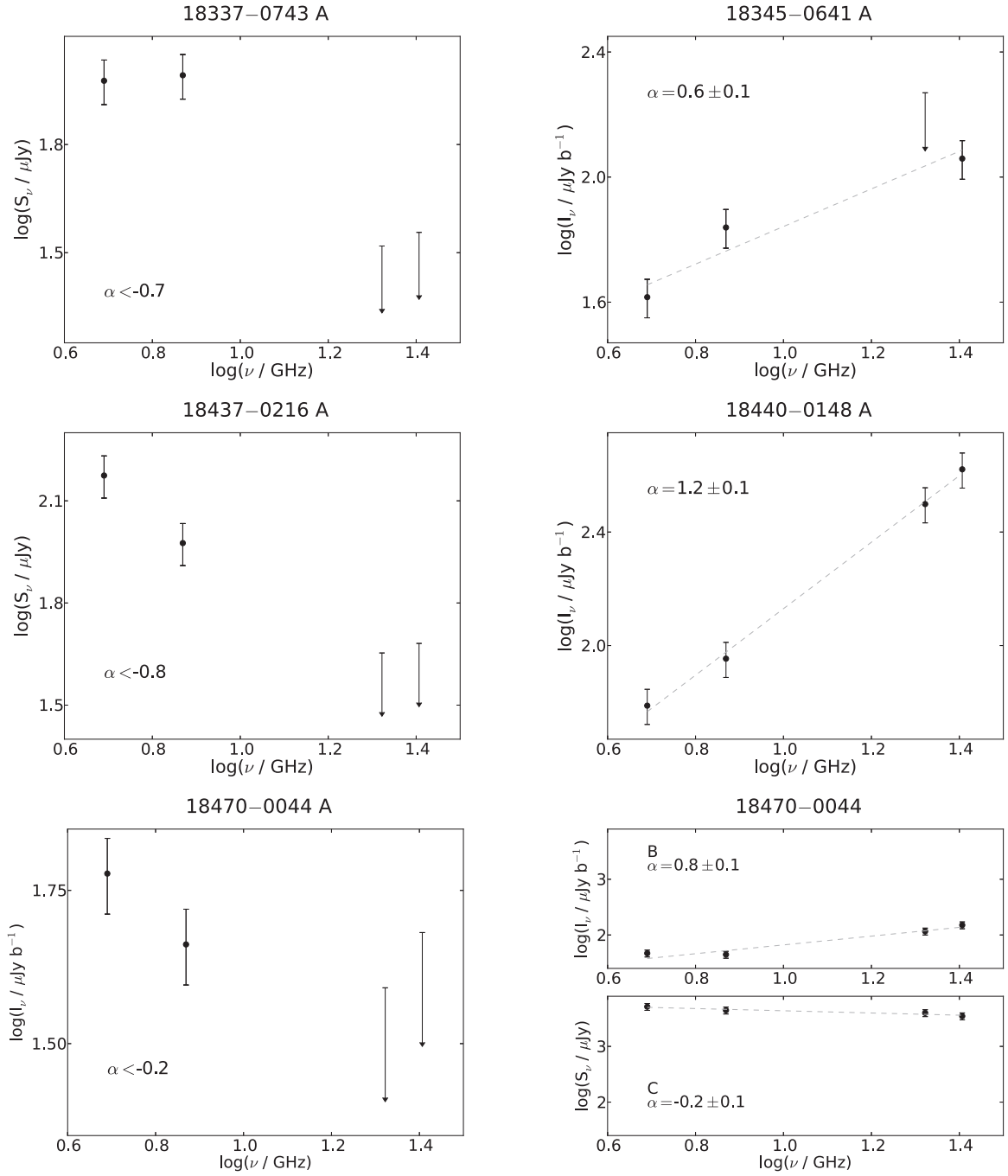

Figure 4 (Continued)

no millimeter size for the clump is available in the literature, we use the FWHM median size for the specific type of clump. Multiple radio sources located closer than 3″ are counted as a single radio source in this histogram. From Figure 3 we see that for HMCs the radio source distribution is strongly peaked toward the center of the millimeter clumps. The median distance of the radio sources from the center of the millimeter dust clumps in HMC sources is 0.06 pc, or about 10^4 au, and the distribution peaks at 0.04 pc, or about 8000 au. For CMC–IR sources we see a flatter distribution, which, due to the lower number of radio detections, could still be consistent with the HMC distribution. In fact, using a Kolmogorov–Smirnov test to compare the spatial offset distribution of the HMCs and CMC–IRs we estimated a p-value = 0.34, i.e., there is no strong evidence that for these two core/clump types the offset distribution is different. Finally, for CMC sources only 1 radio source is detected that is coincident with the dust clumps, thus no statement can be made about their general offset distribution.

3.2. Spectral Indices

Because the observations were made in scaled arrays, the 6 cm and the 1.3 cm images are sensitive to the same angular scales. Hence, these images allow a determination of the source spectral indices α, defined via $S_\nu \propto \nu^\alpha$, independent of source extent. The spectral index for each component was calculated using the flux density at the four central observed frequencies:

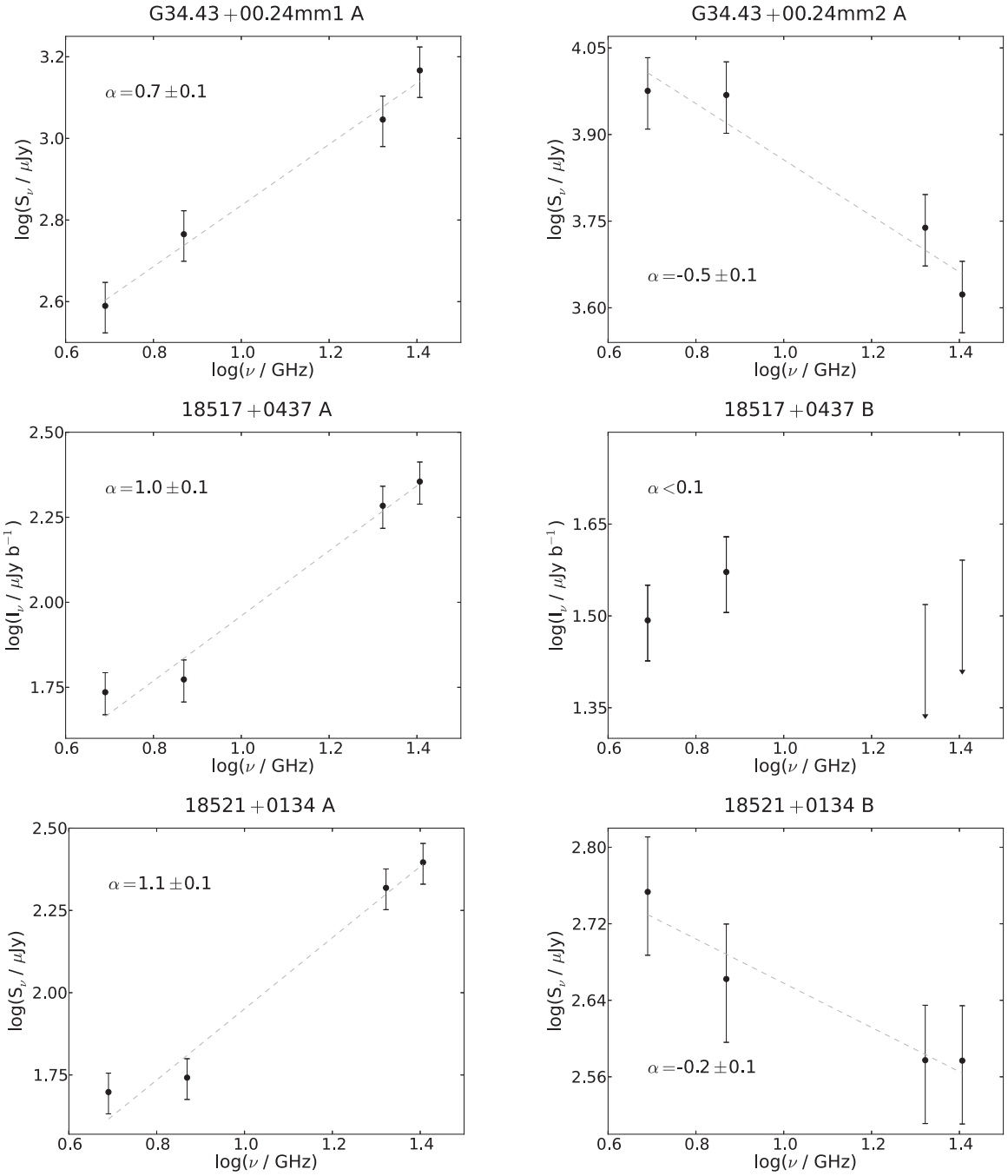

Figure 4 (Continued)

4.9 and 7.4 GHz at 6 cm and 20.9 and 25.5 GHz at 1.3 cm. Therefore, for each source α is calculated over a wide frequency range (~20 GHz), providing a characterization of the frequency behavior of the radio sources, even for low signal-to-noise detections. For very weak sources in the presence of image artifacts, the spectral index was determined using the peak intensity I_ν instead of the total flux density. Figure 4 shows the centimeter SEDs and power-law fits to the data. The uncertainty of the spectral index given by the power-law fit was computed adopting a uniform flux error for all sources. We assumed that the measured flux density (or the peak intensity) is accurate to within 10%, added in quadrature with an assumed 10% error in calibration. These errors are likely underestimated for weak sources, and overestimated for strong sources. Column 10 of Table 4 reports the calculated spectral indices, including the uncertainties for each source. For components not detected at 6 (1.3) cm, a lower (upper) limit in the spectral index is calculated by using a value of S_ν of 3σ. Our calculation assumes that there is no significant source variability in the 3-year interval between the 6 cm observations and half of the observations at 1.3 cm (e.g., Ciliegi et al. 2003). As can be seen in Figure 4, in some cases the spectral behavior of the two data points within an observing band suggests an opposite trend than the derived spectral index. This can be accounted for by a variety of effects, such as calibration errors, image artifacts, etc. Especially for the weakest sources detected just above 5σ we found that in-band spectral indices are not always reliable. Therefore, the spectral index calculated for all

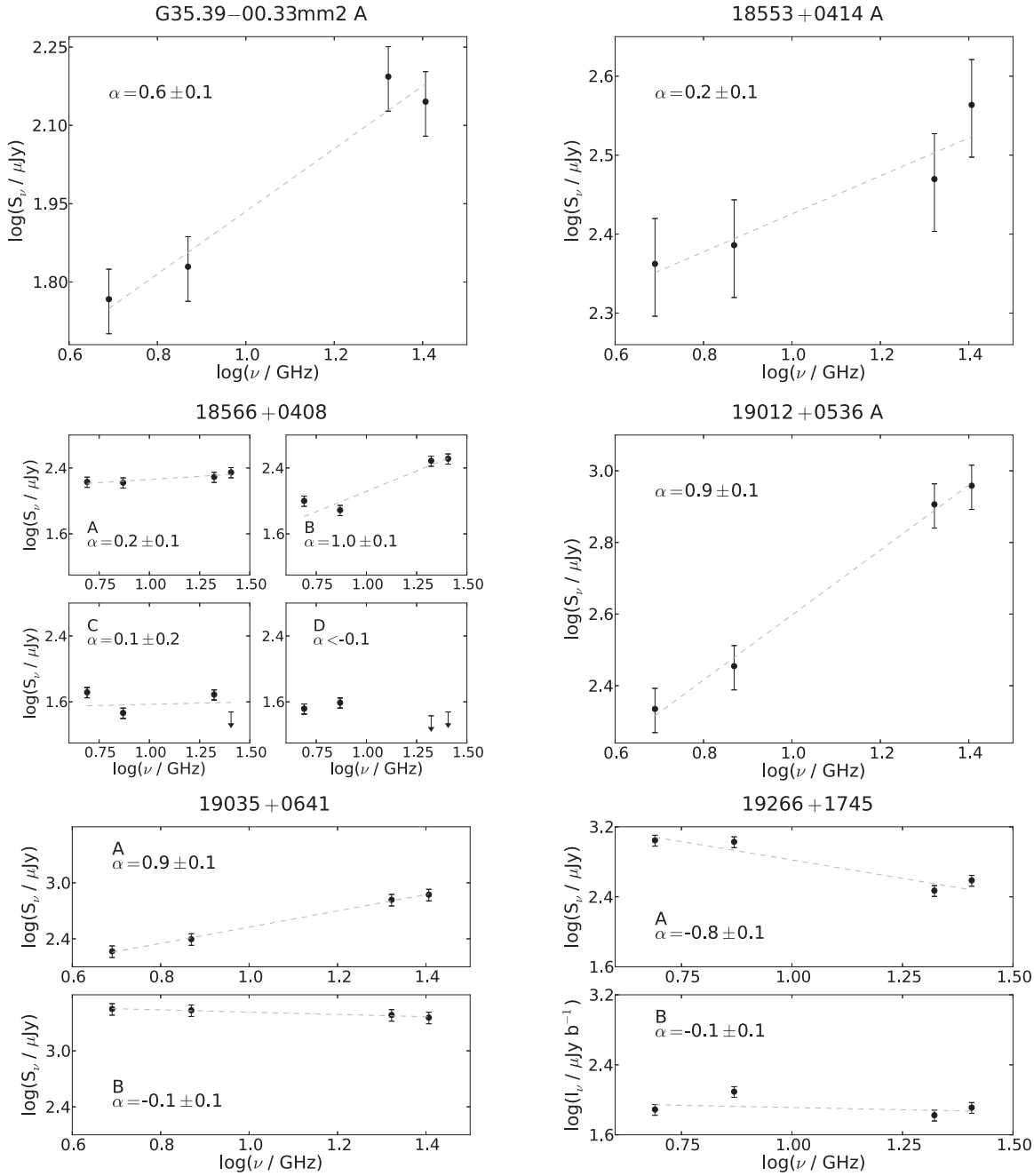

Figure 4 (Continued)

data points over a broader frequency span should provide a better characterization of the spectral behavior of the continuum emission. A further explanation for inconsistencies in the spectral index estimated within an intra-band with respect to the one estimated from the broader band of frequencies could be unresolved sources of opposite spectral behavior within the beam.

Figure 5 shows the distribution of the spectral indices for components within the millimeter clump. The lower and upper limits refer to the estimated α if there is no detection at 6 or 1.3 cm, respectively. The distribution of the detections (i.e., excluding the limits) has a median value of 0.5 and an average value of 0.4, suggesting thermal emission for most sources. These values are consistent with the typical spectral indices found in low-mass thermal radio jets (Anglada et al. 1998). We also note that we detect a significant number of negative spectral indices: the fraction of the detected sources (excluding limits) with a spectral index less than −0.25 is 10%. These latter sources are strong candidates for non-thermal emission.

Thermal free–free emission at centimeter wavelengths in high-mass star-forming regions can have distinct origins, such as H II regions, photoionized internally or externally, ionized accreting flows (Keto 2002, 2003, 2007), stellar winds (Carrasco-González et al. 2015), or shocks produced by the collision of thermal jets with surrounding material (see (Rodríguez et al. 2012) and Sánchez-Monge et al. (2013b) for an extensive list of different ionization processes in high-mass young stellar objects). The non-thermal components

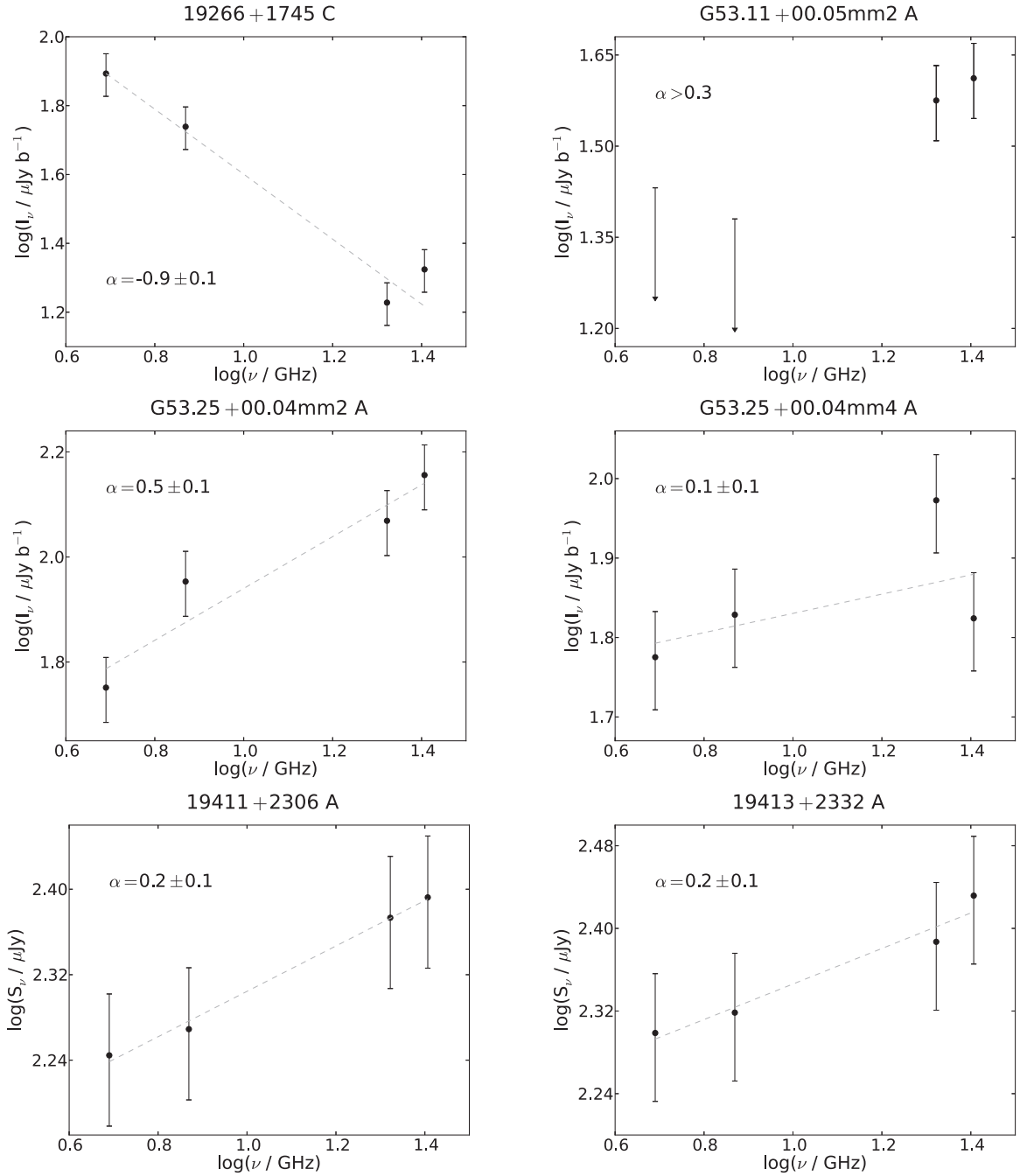

Figure 4 (Continued)

could be protostars with an active magnetosphere (Deller et al. 2013) or high-mass binary stars producing synchrotron radiation in the region where their winds collide (Rodríguez et al. 2012). This emission could also arise from fast shocks in disks and jets, although only a few of these non-thermal jets have been detected (e.g., HH 80-81: Carrasco-González et al. 2010, Serpens: Rodríguez-Kamenetzky et al. 2016). Further discussion of the physical nature of the emission will be presented in Paper II.

3.3. Source Multiplicity

High-mass stars are expected to form mainly in clusters and on average are expected to have more physical companions than low-mass stars. For instance, in Orion the Trapezium cluster has four OB type stars in close proximity, and the companion star fraction of high-mass stars is three times larger than that in low-mass stars (Zinnecker & Yorke 2007). Hence, a key issue in high-mass star formation is the density distribution and the multiplicity in massive clumps. Furthermore, the presence of multiple sources in different evolutionary phases also describes the time sequence of high-mass star formation. In this regard our data show an interesting dichotomy. We detected multiple radio sources primarily for HMCs: about half of HMCs showed two or more radio sources within the FWHM of the millimeter clump, and the other half show single detections. For CMC–IRs, only 20% of the regions with detections have two or more continuum sources within the clump. Another interesting observational result is that 5 out of

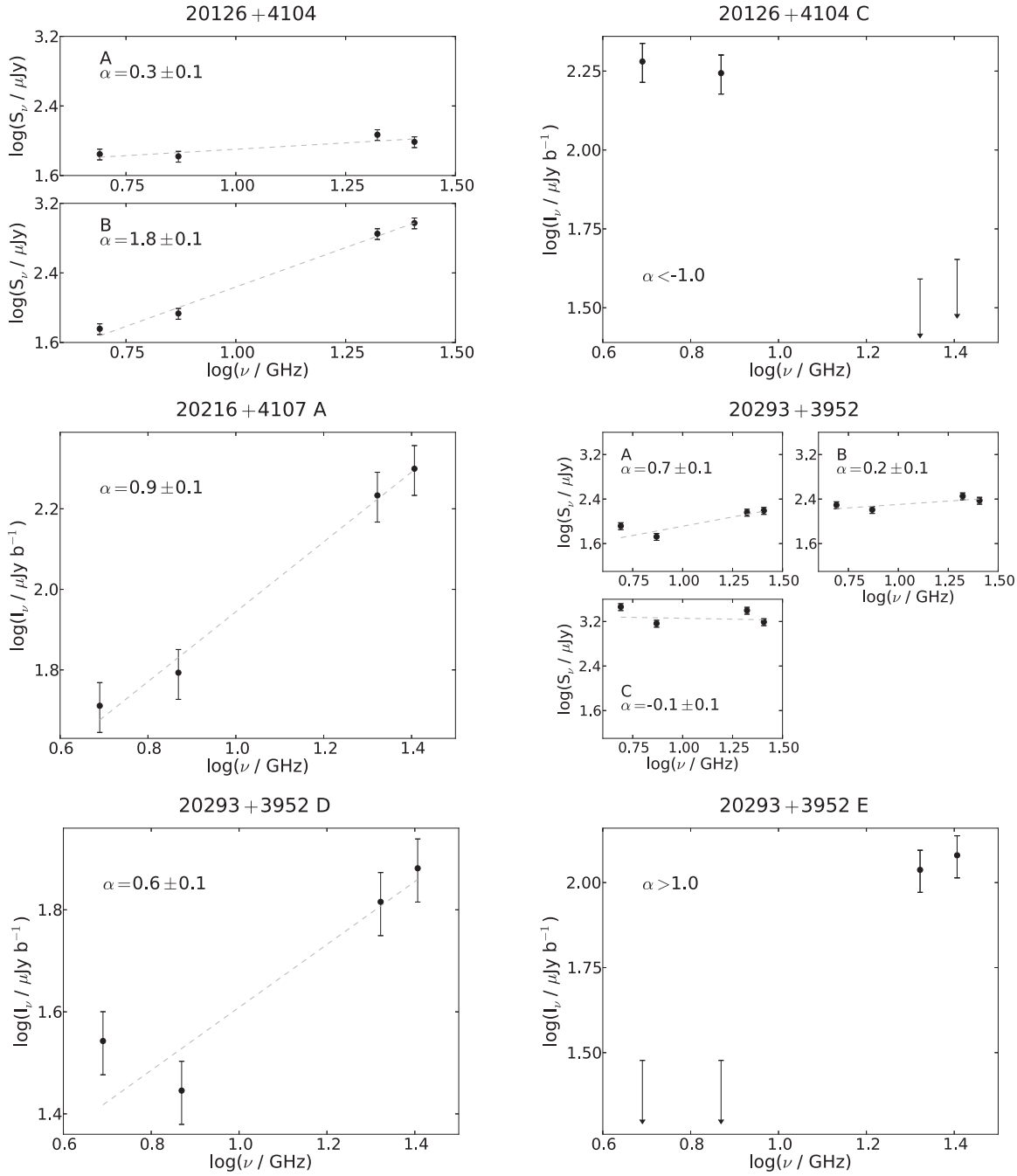

Figure 4 (Continued)

the 25 HMCs observed have an extended radio source reminiscent of a UC H II region (e.g., Wood & Churchwell 1989). These bright and extended radio continuum components are only seen toward the HMCs of our sample. These regions will be discussed further in paper II.

4. SUMMARY

We have carried out deep VLA observations of a radio continuum at 6 and 1.3 cm toward a sample of 58 high-mass star-forming region candidates selected from the literature, and with no previous or relatively weak radio continuum detection at the 1 mJy level. Our sample has been classified according to the infrared properties of the targets and other signposts of star formation activity into three types: CMCs, CMC–IRs, and HMCs. In total, we detected 70 radio sources associated with dusty millimeter clumps in these regions. The detected weak and compact radio sources are prime candidates for high-mass protostars. In this paper we have presented the sample and our observations. Some of the important aspects to highlight from our observations are the following:

1. The detection rates of radio sources associated with the millimeter dust clumps for CMCs, CMC–IRs, and HMCs are 6%, 53%, and 100%, respectively. This result is

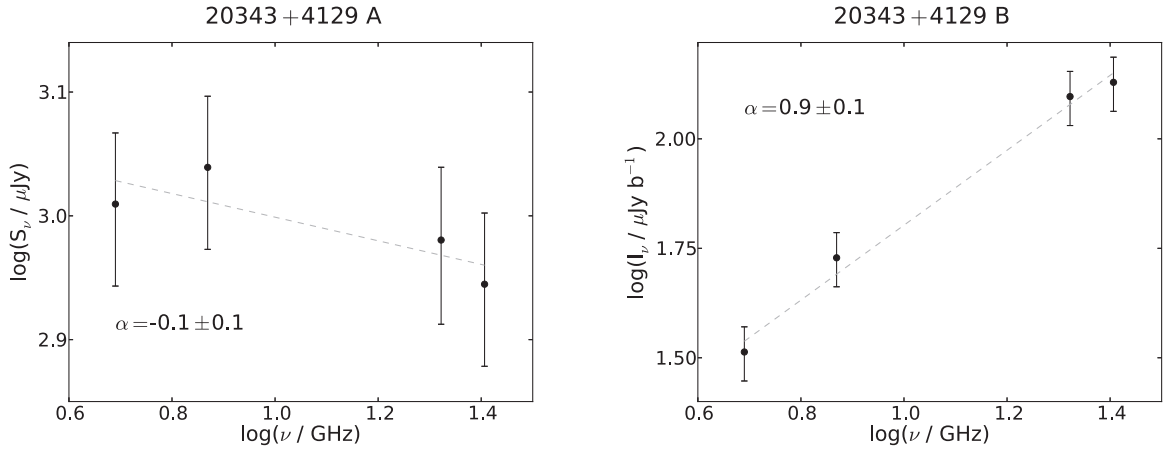

Figure 4 (Continued)

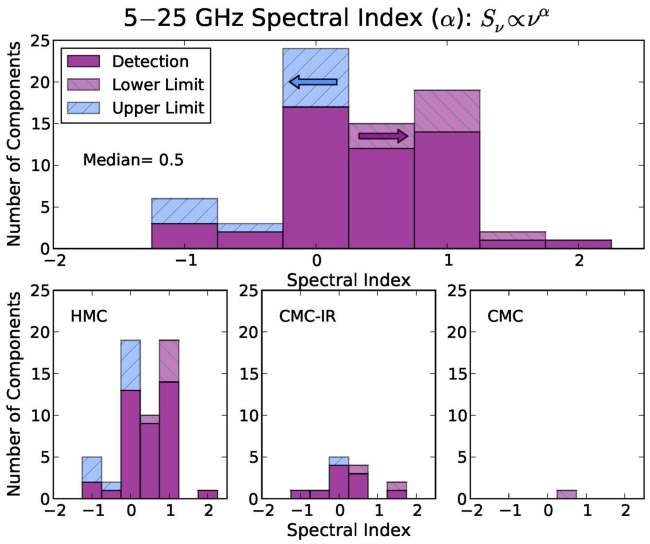

Figure 5. Spectral index (α) distribution of 70 radio sources associated with millimeter clumps, binned in increments of 0.5 in spectral index. If there is no detection at 6 cm, the estimated value of α is a lower limit, and if there is no detection at 1.3 cm, the estimated value for α corresponds to an upper limit. The median value refers only to the detections. The distributions at the bottom show the results independently for each type of clump.

consistent with increasing high-mass star formation activity from CMCs to HMCs.

2. Radio sources located within HMCs and CMC–IR occur close to the dust clump center, with median offsets from the clump center of 10,000 au and 4000 au, respectively.
3. The median 5–25 GHz spectral index for radio sources associated with the millimeter clumps is 0.5, which suggests thermal emission from ionized jets, and is very similar to what is observed in low-mass protostars. Additionally, we found that at least 10% of sources show negative spectral indices, indicative of non-thermal emission.
4. HMCs often have multiple centimeter continuum sources within the surrounding dust clump, whereas CMC–IRs generally have only one or no detectable radio source.

An analysis and discussion of our detections will be presented in Paper II.

We thank H. Beuther for providing 1.2 mm maps for the HMCs in our sample. We thank J. Marvil for stimulating technical discussions about the VLA capabilities. V.R. is supported by the NRAO Grote Reber Doctoral Fellowship. P.H. acknowledges support from NSF grant AST-0908901 for this project. L.L. acknowledges the financial support of CONACyT, Mexico, DGAPA, UNAM, and the von Humboldt Foundation. This research made use of APLpy, an open-source plotting package for Python hosted at http://aplpy.github.com. We thank the anonymous referee whose comments improved this manuscript.

Software: CASA, APLpy.

REFERENCES

AMI Consortium, Davies, M. L., Franzen, T. M. O., et al. 2011, MNRAS, 415, 2708
Anglada, G., Villuendas, E., Estalella, R., et al. 1998, AJ, 116, 2953
Araya, E. D., Hofner, P., Goss, W. M., et al. 2008, ApJS, 178, 330
Beuther, H., Henning, T., Linz, H., et al. 2010, A&A, 518, L78
Beuther, H., Schilke, P., Menten, K. M., et al. 2002a, ApJ, 566, 945
Beuther, H., Schilke, P., Menten, K. M., et al. 2005, ApJ, 633, 535
Beuther, H., Schilke, P., Sridharan, T. K., et al. 2002b, A&A, 383, 892
Brunthaler, A., Reid, M. J., Menten, K. M., et al. 2009, ApJ, 693, 424
Carrasco-González, C., Rodríguez, L. F., Anglada, G., et al. 2010, Sci, 330, 1209
Carrasco-González, C., Torrelles, J. M., Cantó, J., et al. 2015, Sci, 348, 114
Cesaroni, R., Hofner, P., Araya, E., & Kurtz, S. 2010, A&A, 509, A50
Cesaroni, R., Walmsley, C. M., & Churchwell, E. 1992, A&A, 256, 618
Cesaroni, R., Walmsley, C. M., Koempe, C., & Churchwell, E. 1991, A&A, 252, 278
Cesaroni, R. 2005, in IAU Symp. 227, Massive Star Birth: A Crossroads of Astrophysics, ed. R. Cesaroni et al. (Cambridge: Cambridge Univ. Press), 59
Chambers, E. T., Jackson, J. M., Rathborne, J. M., & Simon, R. 2009, ApJS, 181, 360
Chapin, E. L., Ade, P. A. R., Bock, J. J., et al. 2008, ApJ, 681, 428
Chira, R.-A., Beuther, H., Linz, H., et al. 2013, A&A, 552, A40
Ciliegi, P., Zamorani, G., Hasinger, G., et al. 2003, A&A, 398, 901
Cyganowski, C. J., Whitney, B. A., Holden, E., et al. 2008, AJ, 136, 2391
de Zotti, G., Ricci, R., Mesa, D., et al. 2005, A&A, 431, 893
Deller, A. T., Forbrich, J., & Loinard, L. 2013, A&A, 552, A51
Fazal, F. M., Sridharan, T. K., Qiu, K., et al. 2008, ApJL, 688, L41
Fomalont, E. B., Windhorst, R. A., Kristian, J. A., & Kellerman, K. I. 1991, AJ, 102, 1258
Forbrich, J., Schreyer, K., Posselt, B., Klein, R., & Henning, T. 2004, ApJ, 602, 843
Furuya, R. S., Cesaroni, R., Takahashi, S., et al. 2008, ApJ, 673, 363
Garay, G., Rodriguez, L. F., Moran, J. M., & Churchwell, E. 1993, ApJ, 418, 368

Gibb, A. G., & Hoare, M. G. 2007, MNRAS, 380, 246
Goldsmith, P. F., Langer, W. D., & Wilson, R. W. 1986, ApJL, 303, L11
Guzmán, A. E., Garay, G., & Brooks, K. J. 2010, ApJ, 725, 734
Henning, T., Linz, H., Krause, O., et al. 2010, A&A, 518, L95
Hernández-Hernández, V., Zapata, L., Kurtz, S., & Garay, G. 2014, ApJ, 786, 38
Kauffmann, J., & Pillai, T. 2010, ApJL, 723, L7
Keto, E. 2002, ApJ, 568, 754
Keto, E. 2003, ApJ, 599, 1196
Keto, E. 2007, ApJ, 666, 976
Krumholz, M. R., & McKee, C. F. 2008, Natur, 451, 1082
Kurayama, T., Nakagawa, A., Sawada-Satoh, S., et al. 2011, PASJ, 63, 513
Kurtz, S., Cesaroni, R., Churchwell, E., Hofner, P., & Walmsley, C. M. 2000, in Protostars and Planets IV, ed. V. Manning, A. P. Boss, & S. S. Russell (Tuscon, AZ: Univ. of Arizona Press), 299
Kurtz, S., Churchwell, E., & Wood, D. O. S. 1994, ApJS, 91, 659
Linz, H., Krause, O., Beuther, H., et al. 2010, A&A, 518, L123
López-Sepulcre, A., Cesaroni, R., & Walmsley, C. M. 2010, A&A, 517, A66
López-Sepulcre, A., Walmsley, C. M., Cesaroni, R., et al. 2011, A&A, 526, L2
Lu, X., Zhang, Q., Liu, H. B., Wang, J., & Gu, Q. 2014, ApJ, 790, 84
Mezger, P. G., & Henderson, A. P. 1967, ApJ, 147, 471
Molinari, S., Brand, J., Cesaroni, R., & Palla, F. 1996, A&A, 308, 573
Molinari, S., Brand, J., Cesaroni, R., & Palla, F. 2000, A&A, 355, 617
Molinari, S., Brand, J., Cesaroni, R., Palla, F., & Palumbo, G. G. C. 1998, A&A, 336, 339
Molinari, S., Faustini, F., Testi, L., et al. 2008, A&A, 487, 1119
Moscadelli, L., Cesaroni, R., Sánchez-Monge, Á., et al. 2013, A&A, 558, A145
Moscadelli, L., Cesaroni, R., Rioja, M. J., Dodson, R., & Reid, M. J. 2011, A&A, 526, A66
Neufeld, D. A., & Hollenbach, D. J. 1996, ApJL, 471, L45
Nguyen Luong, Q., Motte, F., Hennemann, M., et al. 2011, A&A, 535, A76
Olmi, L., Araya, E. D., Chapin, E. L., et al. 2010, ApJ, 715, 1132
Olmi, L., Cesaroni, R., & Walmsley, C. M. 1993, A&A, 276, 489
Peretto, N., Fuller, G. A., Plume, R., et al. 2010, A&A, 518, L98
Pillai, T., Wyrowski, F., Carey, S. J., & Menten, K. M. 2006a, A&A, 450, 569
Pillai, T., Wyrowski, F., Menten, K. M., & Krügel, E. 2006b, A&A, 447, 929
Purcell, C. R., Hoare, M. G., & Diamond, P. 2008, in ASP Conf. Ser. 387, Massive Star Formation: Observations Confront Theory, ed. H. Beuther, H. Linz, & T. Henning (San Francisco, CA: ASP), 389
Rathborne, J. M., Garay, G., Jackson, J. M., et al. 2011, ApJ, 741, 120
Rathborne, J. M., Jackson, J. M., Chambers, E. T., et al. 2010, ApJ, 715, 310
Rathborne, J. M., Jackson, J. M., & Simon, R. 2006, ApJ, 641, 389
Reid, M. J., Argon, A. L., Masson, C. R., Menten, K. M., & Moran, J. M. 1995, ApJ, 443, 238
Reid, M. J., Menten, K. M., Greenhill, L. J., & Chandler, C. J. 2007, ApJ, 664, 950
Rodríguez, L. F., González, R. F., Montes, G., et al. 2012, ApJ, 755, 152
Rodríguez-Kamenetzky, A., Carrasco-González, C., Araudo, A., et al. 2016, ApJ, 818, 27
Rosero, V., Hofner, P., McCoy, M., et al. 2014, ApJ, 796, 130
Sakai, T., Sakai, N., Furuya, K., et al. 2012, ApJ, 747, 140
Sánchez-Monge, Á., Beltrán, M. T., Cesaroni, R., et al. 2013a, A&A, 550, A21
Sánchez-Monge, Á., Kurtz, S., Palau, A., et al. 2013b, ApJ, 766, 114
Sánchez-Monge, Á., Palau, A., Fontani, F., et al. 2013c, MNRAS, 432, 3288
Sánchez-Monge, Á., Pandian, J. D., & Kurtz, S. 2011, ApJL, 739, L9
Sanhueza, P., Jackson, J. M., Foster, J. B., et al. 2012, ApJ, 756, 60
Sanna, A., Cesaroni, R., Moscadelli, L., et al. 2014, A&A, 565, A34
Sato, M., Wu, Y. W., Immer, K., et al. 2014, ApJ, 793, 72
Shepherd, D. S., & Churchwell, E. 1996, ApJ, 457, 267
Smith, H. A., Hora, J. L., Marengo, M., & Pipher, J. L. 2006, ApJ, 645, 1264
Sridharan, T. K., Beuther, H., Schilke, P., Menten, K. M., & Wyrowski, F. 2002, ApJ, 566, 931
Tanaka, K. E. I., Tan, J. C., & Zhang, Y. 2016, ApJ, 818, 52
Wilson, T. L., Boboltz, D. A., Gaume, R. A., & Megeath, S. T. 2003, ApJ, 597, 434
Wood, D. O. S., & Churchwell, E. 1989, ApJ, 340, 265
Wu, Y. W., Sato, M., Reid, M. J., et al. 2014, A&A, 566, A17
Xu, Y., Moscadelli, L., Reid, M. J., et al. 2011, ApJ, 733, 25
Zhang, Q., Hunter, T. R., Brand, J., et al. 2001, ApJL, 552, L167
Zhang, Q., Sridharan, T. K., Hunter, T. R., et al. 2007, A&A, 470, 269
Zinnecker, H., & Yorke, H. W. 2007, ARA&A, 45, 481